AIAA JOURNAL
Vol. 50, No. 12, December 2012

Fluid–Thermal Response of Spherical Dome Under a Mach 6.59 Laminar Boundary Layer

Christopher M. Ostoich,* Daniel J. Bodony,† and Philippe H. Geubelle‡
University of Illinois at Urbana-Champaign, Illinois 61801

DOI: 10.2514/1.J051634

The coupled fluid–thermal response of a nominally rigid aluminum spherical dome fixed to a ceramic panel holder placed in a Mach 6.59 laminar boundary layer is examined. The compressible Navier–Stokes equations for a thermally perfect gas and the transient heat equation in the structure are solved simultaneously using two high-fidelity solvers coupled at the solid–fluid interface. The geometry and flow conditions correspond to those investigated in the 8-Foot High Temperature Tunnel at NASA Langley during testing of metallic thermal protection systems for the National Aerospace Plane for which experimental heat flux data are available. Predicted surface heat fluxes are within 10% of the measured values in the dome interior with greater differences found near the dome edges where uncertainties concerning the experimental model's construction likely influence the thermal dynamics. On the flat panel holder, the local surface heat fluxes approach those on the windward dome face due to a dome-induced horseshoe vortex scouring the panel's surface. Comparisons with simpler models of heat transfer indicate they fail to be accurate in regions where the dome-influenced flow impacts the ceramic panel. Cumulative effects of flow-thermal coupling at later simulation times on panel drag and surface heat transfer are quantified.

Nomenclature

A, Λ	=	Roe matrix, diagonalized Roe matrix
C_p	=	specific heat capacity at constant pressure, J/kg · K
C_v	=	specific heat capacity at constant volume, J/kg · K
c	=	isentropic speed of sound, $\sqrt{\gamma p/\rho}$, m/s
F	=	divergence of the fluxes
$\boldsymbol{g}$	=	boundary data
J	=	Jacobian
k	=	thermal conductivity, W/m · K
N	=	sponge amplitude
ϵ	=	heat flux convergence value, W/m^2
P, Q, E_1	=	SBP operator matrices
p	=	thermodynamic pressure, Pa
Pr	=	Prandtl number, $C_p\mu/k$
$\boldsymbol{q}$	=	vector of conserved variables $(\rho, \rho u_i, \rho E)^T$
q_j	=	fluid heat flux vector, $-k\partial T/\partial x_j$, W/m^2
$\boldsymbol{R}$	=	characteristic variables
R	=	specific gas constant
Re	=	Reynolds number, $\rho_\infty a_\infty L/\mu_\infty$
T	=	thermodynamic temperature, K
t	=	time, s
$\boldsymbol{u}$	=	velocity, $(u, v, w)^T$, m/s
$\hat{U}$	=	boundary normal velocity, m/s
$\boldsymbol{x}$	=	spatial coordinates, $(x, y, z)^T$, m
α_f	=	filter strength parameter
γ	=	ratio of specific heats, C_p/C_v
δ_{ij}	=	Kronecker delta
η	=	sponge zone forcing term
κ	=	thermal diffusivity, $k/\rho C_p$, m^2/s
μ, λ	=	first and second coefficients of fluid viscosity, kg/m · s
$\boldsymbol{\xi}$	=	computational coordinates, $(\xi, \eta, \zeta)^T$
ρ	=	density (kg/m^3)
ρE	=	total energy, $\rho e + \frac{1}{2}\rho u_i u_i$ (J/m^3)
ρe	=	internal energy (J/m^3)
τ_{ij}	=	viscous stress tensor, $\mu(\partial u_i/\partial x_j + \partial u_j/\partial x_i) + \lambda\partial u_k/\partial x_k\delta_{ij}$, N/m^2
σ	=	simultaneous-approximation-term penalization parameters
ϕ	=	methane–air equivalence ratio
χ	=	rotation matrix

Subscripts

i, j	=	direction index
m	=	time step index
n	=	normal
ref	=	reference condition
w	=	wall
∞	=	free-stream condition

Superscripts

$I1$	=	inviscid data
$I2$	=	viscous data
$+$, $+$	=	incoming variables, wall variables

Presented at the 41st AIAA Fluid Dynamics Conference and Exhibit, Honolulu, Hawaii, June 27–June 30, 2011; received 22 September 2011; revision received 12 March 2012; accepted for publication 25 April 2012.

*Graduate Student, Department of Aerospace Engineering, 306 Talbot Laboratory, MC-236. Student Member AIAA.

†Assistant Professor, Department of Aerospace Engineering, 306 Talbot Laboratory, MC-236; bodony@illinois.edu. Senior Member AIAA (Corresponding Author).

‡Professor, Department of Aerospace Engineering, 306 Talbot Laboratory, MC-236. Member AIAA.

I. Introduction

FUTURE high-performance United States Air Force (USAF) vehicles are expected to be lightweight, flexible, and reusable. These vehicles will likely be fitted with powerful propulsion systems whose exhaust will impact portions of the vehicle's skin, either on external mold lines or in buried engine exhaust ducts. As a result, large loads will be applied to relatively thin-walled panels, potentially leading to significant fluid–thermal-structural coupling. Subsequently, portions of the vehicle will be exposed to environments that will lead to severe fatigue design requirements. For example, Fig. 1 outlines the three main fatigue risk areas identified in a National Aerospace Plane (NASP)–era study for a generic hypersonic vehicle [1,2]; namely, the 1) inlet ramp, 2) exhaust ramp,

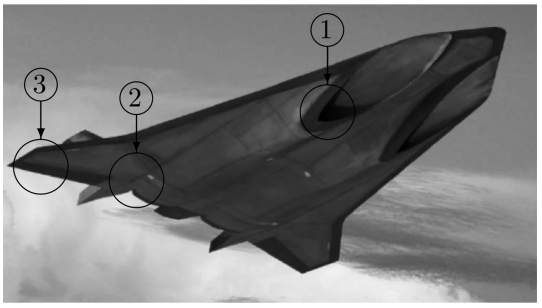

Fig. 1 Generic hypersonic vehicle showing regions of significant thermoacoustic fatigue risk.

and 3) control surfaces. For a reusable, lightweight hypersonic vehicle to be feasible, different design paradigms are required, including a renewed focus on lightweight flexible and hot structural design and full vehicle systems integration. Moreover, the acceptable amount of conservative design margins will be significantly reduced due to weight constraints, leading to reduced design tolerances and more emphasis on accurate, reduced-order models for design [3].

Design methodologies against flow-induced fatigue use a variety of (semi-)empirical techniques that have been honed over time using a combination of analytical approximations [4–6], experimental data [7,8], and parameter tuning [9]. As vehicle performance envelopes expand, the semi-empirical models break down and lead to either overly conservative, heavy designs or, worse, underdesigned elements. In recent years, the F/A-18 [10] (lower nacelle skin) and B-2 [11] (exhaust aft deck) have each suffered from propulsion-load-induced fatigue resulting in reduced operational availability.

Prevention against further thermoacoustic fatigue issues requires that the design methodologies be updated. A step in this direction is the inclusion of nonlinear interactions in the modal descriptions of the underlying structure to permit thermoelastic effects, membrane stresses, and larger amplitude vibrations [12–15], an approach being followed at the Air Force Research Laboratory (AFRL) and at NASA Langley. Finite element formulations are used to develop an in vacuo modal description of the structure; however, the propulsion-induced loads are still based on experimental data taken recently at AFRL [14] in a simulated environment subelement facility (SEF) or on older data taken at NASA [7,8], for example.

There is, thus, a fundamental disconnect in the current prediction methods; although acoustic fatigue is a thermoacoustic–structure interaction problem, the models are built using independent components for the thermal, acoustic, and structural fields at simulated, but not actual, conditions. When high-speed flow is present, the situation is worse, as there are limited experimental facilities capable of simulating a thermoelastic material in the presence of hypersonic flow. A decade ago, the National Research Council (NRC) noted that the lack of on-ground testing capability at flight-realistic hypersonic conditions was a limiting factor in high-speed vehicle development, so much so that additional focus should be placed on analysis tools used in the vehicle definition process [16].

For the range of environments in which sonic fatigue and/or aerothermoelastic coupling are an issue, there are limited computational and experimental facilities to accurately assess the loading scenarios a structural element will experience at realistic flight conditions. A nonuniform thermal field and/or high-speed grazing flow further complicates matters. Of particular interest is the amount of coupling required in predictive methods between the fluid, thermal, and structural domains for a given level of confidence. Recent results suggest that the coupling required is a strong function of the vehicle Mach number [17].

At present, full-order coupled analysis can be prohibitive due to computational cost, especially when long time records are desired. To mitigate the cost of the coupled approach, various reduced-order models (ROMs) have been used to investigate the effects of coupling, physical loads, and design requirements for hypersonic flight. Various types of ROMs have been developed, oftentimes using full-order approaches for one branch of the coupled analysis and reduced-order approaches for the others. For example, Culler and McNamara [18] developed a coupled framework that uses third-order piston theory [19] coupled with Eckert's reference enthalpy method [20] to predict fluid aerodynamic pressure and thermal loads, and methods of varying fidelity for the thermal and structural solutions for thin panels. For their flight profile, they found the mutual interaction between structural deformation and aerodynamic heating to be significant, especially over increased time records [18]. They also found that quasi-static, time-averaged dynamic coupling and instantaneous dynamic coupling yield identical flutter boundaries, but thermal stresses and temperature varying material properties altered flutter boundaries [17].

Another class of ROMs uses snapshots of full-order, steady-state solutions to provide additional information. Crowell and McNamara [21] computed sample steady-state Reynolds averaged Navier–Stokes (RANS) solutions that were then corrected for unsteady flow effects using third-order piston theory. They found this approach improved predictions significantly when compared to the use of piston theory or Euler solutions, stressing the importance of viscous effects in hypersonic flows. In the same work, they investigated the use of a database of steady-state computational fluid dynamics (CFD) snapshots either to create an optimal basis of the solution space using proper orthogonal decomposition (POD), or to make approximations to the solution by interpolating between snapshots using kriging. It was found that both approaches yielded average L_∞ errors around 5% and maximum errors of 10–20%. The kriging models were found to be slightly more accurate, whereas the POD models were more computationally efficient. Falkiewicz and Cesnik [22] considered the use of POD to provide a reduced-order thermal solution in aerothermoelastic simulations. This approach approximated the full-order solution with an average error of 8.2% when the thermal load on the structure was known a priori.

Increasing computational capabilities have enabled full-order coupled approaches to make structural response predictions in hypersonic environments. Dechaumphai et al. [23] used an integrated fluid–thermal–structural approach to analyze the response of a two-dimensional leading edge in a Mach 6.47 uniform flow. They noted that the fluid–thermal coupling from the increase in the leading edge temperature resulted in significant reduction in aerodynamic heating. Thermomechanical results of an engine inlet cowl subject to a prescribed heat load simulating a shock–shock interference produced severe in-plane stresses, suggesting the need for three-dimensional simulations. In a later work, Dechaumphai et al. [24] investigated the engine inlet cowl while computing the shock–shock interference thermal load using a two-dimensional finite element Navier–Stokes solver. The pressure at the interference location matched the experiment, but the heat load, as predicted using a two-point differencing approximation, was only one-third of the experimentally measured values, despite a very small wall normal distance of the first element in the fluid domain. Thornton and Dechaumphai [25] used the previously mentioned two-dimensional finite element fluid–thermal–structural solver to study hypersonic flow over metallic thin panels in both aligned and inclined configurations with respect to the freestream. Results showed that even very modest deformations altered flow features and introduced shocks, expansions, and recirculation regions that significantly influenced the heat load.

Using a sequential approach, a numerical simulation of thermal protection system (TPS) panel bowing was performed by Kontinos and Palmer [26]. The semi-empirical methodology used CFD results that were computed a priori to form a surface heating distribution function parameterized by dome deflection height. Using this approach, they found that the dome deflection height did not change due to the surface heating perturbation caused by the thermal bowing of the dome into the flow. This is contradictory to what Culler and McNamara [27] found using their more strongly coupled ROM approach. Hassan et al. [28] used two-dimensional coupled CFD, material thermal response, and flight dynamics solvers to study the coupled effects of a nonequilibrium flow on the flight trajectory of a vehicle with an ablating surface. They saw that as the simulation progressed, the nose tip blunted due to ablation, affecting the flow

and indicating that, after more time, the coupled and uncoupled results would diverge from each other.

Recently, Crowell et al. [29] investigated the fluid–thermal coupling requirements to make heat load predictions on a panel under shock-turbulent boundary layer interactions (STBLIs). Their findings showed that movement of the shock location due to a prescribed panel motion significantly altered the aerothermal load on the panel. Results also suggested that quasi-static fluid–thermal temporal coupling is a viable option for response prediction. Zhao et al. [30] performed a three-dimensional coupled simulation on a leading edge in Mach 6.47 flow using a Riemann solver with a k-ϵ-R turbulence model coupled with finite element thermal and structural solvers. They showed that a wall normal resolution of $y^+ \leq 5$ was required for accurate prediction of the heat load when compared with experimental results, and that the effect of the flow-thermal coupling on the aerodynamic heating was significant.

In the present work, a high-accuracy, high-fidelity coupled fluid–thermal methodology is developed and is used to examine a Mach 6.59 experiment in the NASA Langley 8-Foot High Temperature Tunnel [31]. The simulation uses a globally fifth-order accurate finite difference discretization in space in the fluid domain to resolve flow features that might influence structural response in a hypersonic environment. Both calorically and thermally perfect gases are considered. The thermal domain includes a rigid dome protuberance and spatially varying material properties. The goals of this study are 1) to make a quantitative comparison with thermal measurements from a well-documented hypersonic wind tunnel experiment, and 2) to evaluate the consequences and gains of using a high-order, high-fidelity approach in investigating structural response in a hypersonic environment. In the work surveyed previously, the structural response in extreme environments has been studied using a variety of approaches ranging from coupled ROMs simulating representative aerospace structures [17,22,27,32,33] to more direct methods studying flows over two-dimensional [28,29] and three-dimensional [30] shapes. The current work uses a three-dimensional, high-fidelity coupled approach utilizing accurate numerical schemes to study the thermal response of a realistic aerospace structure in a hypersonic flow to demonstrate the limitations of simplified approaches commonly used, and to assess the difficulties associated with multiphysics validation.

II. Solvers

A. Fluid Domain

Our fluid model describes the motion of a fully nonlinear, compressible, viscous, calorically or thermally perfect gas. The Navier–Stokes equations describe conservation of mass, momentum, and total energy and are given as

$$\begin{aligned}\frac{\partial \rho}{\partial t} + \frac{\partial}{\partial x_i}(\rho u_i) &= 0,\\ \frac{\partial \rho u_i}{\partial t} + \frac{\partial}{\partial x_j}(\rho u_i u_j + p\delta_{ij} - \tau_{ij}) &= 0,\\ \frac{\partial \rho E}{\partial t} + \frac{\partial}{\partial x_j}[(\rho E + p)u_j + q_j - u_i\tau_{ij}] &= 0\end{aligned} \tag{1}$$

where repeated indices are summed. We solve Eq. (1) on a nonuniform, nonorthogonal mesh defined by the smooth mappings

$$\boldsymbol{x} = \boldsymbol{X}(\boldsymbol{\xi}), \quad \text{with inverse } \boldsymbol{\xi} = \boldsymbol{\Xi}(x)$$

where $\boldsymbol{X}^{-1} = \boldsymbol{\Xi}$ and Jacobian $J = |\partial \boldsymbol{X}/\partial \boldsymbol{\Xi}|$. It can be shown that Eq. (1) maps into an equivalent conservative form in the computational variable $\boldsymbol{\xi}$ [34].

Finite differences are used to approximate the spatial derivatives in the computational coordinates. We use the summation-by-parts operators [35,36], which, when coupled to the simultaneous-approximation-term (SAT) boundary conditions [37–40], yield a provably stable and accurate method [41]. The spatial approximation to $\partial/\partial\xi$ is $P^{-1}Q$, where Q has the property $Q + Q^T = \mathrm{diag}(-1, 0, \ldots, 0, 1)$. For the SAT formulation, which is a penalization approach, a penalty term is added to the right-hand side of the governing equations. Following the notation in Svärd and Nordström [39], the penalized equation is

$$\frac{\partial \boldsymbol{q}}{\partial t} = \mathcal{F}(\boldsymbol{q}) + \sigma^{I1} P^{-1} E_1 A^+ (\boldsymbol{q} - \boldsymbol{g}^{I1}) + \frac{\sigma^{I2}}{Re} P^{-1} E_1 I (\boldsymbol{q} - \boldsymbol{g}^{I2}) \tag{2}$$

where σ^{I1} and σ^{I2} are the penalty parameters for the inviscid and viscous boundary conditions, respectively, and $E_1 = (1, 0, \ldots, 0)^T$. Here, $\mathcal{F}(\boldsymbol{q})$ represents the divergence of the fluxes in the governing equations, A^+ is a Roe matrix to be defined later, and $\boldsymbol{I}$ is the identity matrix. It is known that $\sigma^{I1} \leq -2$ and

$$\sigma^{I2} \leq -\frac{1}{4P(1,1)} \max\left(\frac{\gamma\mu}{Pr\rho}, \frac{5\mu}{3\rho}\right) \tag{3}$$

are required for numerical stability. In the current work, both σ^{I1} and σ^{I2} are set to -2. The boundary data are contained in the vectors $\boldsymbol{g}^{I1}$ and $\boldsymbol{g}^{I2}$. For inviscid flows, one omits the second penalty term and defines the target vector by

$$\boldsymbol{g}^{I1} = \begin{bmatrix} \rho \\ \rho(\boldsymbol{u} - [(\boldsymbol{u}\cdot\boldsymbol{n}) - (\boldsymbol{u}_w \cdot \boldsymbol{n})]\boldsymbol{n}) \\ \rho e + \frac{1}{2}\rho|\boldsymbol{u} - [(\boldsymbol{u}\cdot\boldsymbol{n}) - (\boldsymbol{u}_w \cdot \boldsymbol{n})]\boldsymbol{n}|^2 \end{bmatrix} \tag{4}$$

The matrix $A^+ = \chi\Lambda^+\chi^{-1}$ selects only the incoming characteristic variables $\boldsymbol{R} = \chi\boldsymbol{q}$, where χ transforms the conserved variable $\boldsymbol{q}$ to characteristic variable $\boldsymbol{R}$. For a calorically perfect gas, χ is given by Pulliam and Chaussee [42]; however, for a thermally perfect gas, χ is found numerically. In both cases, χ is evaluated using the Roe average of $\boldsymbol{q}$ and $\boldsymbol{g}^{I1}$. $\Lambda^+ = \Lambda - |\Lambda|$ is a diagonal matrix containing the elements $\Lambda = \mathrm{diag}\{\hat{U}, \hat{U}, \hat{U} + c, \hat{U} - c\}|\nabla_x\xi|$ where $\hat{U}$ is the component of the velocity in the wall normal direction ($\boldsymbol{n} = \nabla_x\xi/|\nabla_x\xi|$), For the viscous penalty term, the target data are

$$\boldsymbol{g}^{I2} = [\rho, \rho\boldsymbol{u}_w, \rho e(T_w) + \frac{1}{2}\rho|\boldsymbol{u}_w|^2]^T \tag{5}$$

which applies a no-slip, isothermal condition for a moving wall with velocity $\boldsymbol{u}_w(\boldsymbol{x}, t)$ and with temperature $T_w(\boldsymbol{x}, t)$. Additionally, sponge regions, where the forcing term $-\eta(\boldsymbol{q} - \boldsymbol{q}_{\mathrm{ref}})$ is added to the right-hand side of Eq. (1) , are employed. The effect is to absorb and minimize reflections from computational boundaries by penalizing the difference between the internal solution $\boldsymbol{q}$ and a target solution $\boldsymbol{q}_{\mathrm{ref}}$ [43]. The strength of the penalization is controlled by $\eta(\xi) = N\xi^2$, where N is the sponge amplitude and ξ is the distance from the boundary normalized by the sponge length. The effect of the sponge zones can be seen in Fig. 2a. The zones affected by the sponge have been removed from the remaining figures in this paper to clarify the presentation of the solution (for example, Fig. 2b).

For the current work, the strong form of the viscous terms is utilized in which spatial second derivatives are approximated by repeated application of first derivative finite difference operators. This method is more computationally efficient than the weak form (expanded second derivatives). However, the strong form of the viscous terms has no numerical damping at the highest wave number, which can lead to instabilities in the simulation. The implicit filter presented by Lele [44] is used to provide numerical damping to the solution at each time step. Filtering is accomplished by solving the linear system of equations resulting from the application of Eq. (6) to grid points i in each direction:

$$\begin{aligned}\alpha_f\hat{f}_{i-1} + \hat{f}_i + \alpha_f\hat{f}_{i+1} = af_i + \frac{d}{2}(f_{i+3} + f_{i-3})\\ + \frac{c}{2}(f_{i+2} + f_{i-2}) + \frac{b}{2}(f_{i+1} + f_{i-1})\end{aligned} \tag{6}$$

where $\hat{()}$ denotes a filtered quantity and a, b, c, and d determine the accuracy of the filter and are functions of α_f. The parameter α_f governs the filter strength, which diminishes as $\alpha_f \to 0.5$, and was

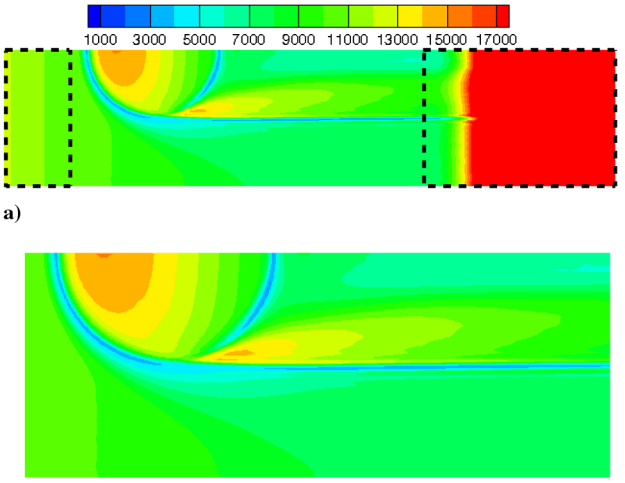

Fig. 2 Surface heat flux (W/m^2) at $t = 1$ s: a) with sponge zones, and b) without sponge zones. Sponge zones are omitted from remaining figures.

chosen as 0.499 for the simulations presented hereafter. To minimize the oscillations due to the presence of shocks in the fluid domain, the shock capturing scheme of Kawai et al. [45] is used. Any direct effect of the scheme on the calculation of heat flux into the thermal domain was removed by allowing only the artificial bulk viscosity to be modified. The shock capturing scheme was seen to have no effect on the surface heat flux.

Both calorically perfect (constant specific heat capacities) and thermally perfect (temperature-varying specific heat capacities) gas models were used. The thermally perfect model, which departs from the calorically perfect assumption at high temperatures, was implemented using a user-provided lookup table. For the current work, the thermal properties of methane–air combustion products are given in Leyhe and Howell [46].

The fluids code has been used in a variety of fluid-only problems involving both laminar and turbulent flows [47–52]. The temporal advancement of Eq. (1) is deferred to a later section.

B. Thermal Domain

The thermal solution in the solid is found by solving the three-dimensional transient heat conduction equation

$$\rho C_p \frac{\partial T}{\partial t} = \frac{\partial}{\partial x_j}\left(k \frac{\partial T}{\partial x_j}\right) \tag{7}$$

using an in-house finite element thermal code fitted with linear basis functions on a hexahedral mesh. The solution is marched implicitly in time using the second-order accurate, unconditionally stable Crank–Nicholson scheme [53]. The resulting linear system of equations is then solved iteratively using the generalized minimum residual (GMRES) [54] method provided in the HYPRE [55] suite of parallel linear algebraic solvers. The thermal solver has been verified against classical analytical solutions.

C. Interface Treatment

The individual codes are weakly coupled at the interface where the fluid–thermal interaction takes place. The fluid and thermal solutions are found independently in their respective domains at a given time step $t_m = m\Delta t$. The spatial transfer along the interface is achieved using the common refinement scheme, which provides a conservative and accurate transfer of heat flux across the nonmatching discretizations at the interface [56,57]. The stability benefits of the implicit thermal solver are exploited in the choice of the physical quantities to pass at the fluid–thermal interface. An analysis by Giles [58] showed that numerical stability is increased when temperature is passed from the solid to the fluid while the heat flux is passed from the fluid to the solid. Roe et al. [59] extended this analysis to problems involving moving grids. Thus, the thermal solver provides $T_w(\boldsymbol{x}, t)$ to the fluid solver while $q_n = -k\Delta T \cdot \boldsymbol{n}$, where $\boldsymbol{n}$ is the unit normal pointing into the fluid from the solid, is determined by the fluid and transferred to the solid thermal solver.

D. Temporal Solution Procedure

One major challenge in fluid–thermal interaction simulations is the impact of the highly disparate time scales involved in fluid and thermal physics. In preliminary work [60], the fluid solution was seen to recover a state of mechanical equilibrium roughly 1 ms after a boundary condition perturbation. The thermal solution, as presented later in this report, changes on the order of 1–10 K/s in the region of interest. This results in an $\mathcal{O}(10^2)$–$\mathcal{O}(10^3)$ ratio between the thermal and fluid time scales. The computational cost associated with resolving the time scales involved in both disciplines can be prohibitive due to the fact that the transient thermal solution in the solid evolves much more slowly than does the solution in the fluid. This effect is exacerbated in the case where the fluid solution is explicitly advanced in time, in which the coupled system time step is limited by the stability requirements associated with the fluid solution. However, the goal of the current work is to determine the transient thermal response of a structure in the hypersonic environment with a laminar boundary layer. In this situation, it is not necessary to resolve the small time scales in the fluid solution. The transient solution of the fluid–thermal system becomes more tractable if a quasi-static temporal coupling is employed. The time-accurate thermal solution at the $m + 1$ time step is found by integrating the solution given the thermal load provided by the fluid solution at time step m. The interface temperature is given as a boundary condition in the fluid domain and the fluid is marched from time step m to the steady-state solution consistent with the $m + 1$ interface temperature.

Because a temporally accurate fluid solution is not required, the equations [Eq. (1)] can be integrated to steady state using a less accurate, accelerated method, such as the five-stage Runge–Kutta (RK5) scheme developed by Jameson [61]. In the RK5 scheme, the viscous fluxes are evaluated at two of the five stages and are frozen for the remaining stages. These schemes were shown by Swanson and Turkel [62] to extend the stability limit significantly while sacrificing temporal accuracy. The variant used in the current work evaluates the viscous terms in the first two stages and is formally first-order accurate in Δt.

III. Coupled Fluid-Thermal Solver Validation

As mentioned previously, one key factor that makes simulation of the hypersonic environment so attractive is that it is difficult to run experiments that replicate the desired conditions. Unfortunately, because of this fact, experimental data needed to validate the solutions produced by numerical simulations of extreme environments are limited. However, in the 1980s, researchers at NASA Langley conducted a series of hypersonic wind tunnel experiments that investigated the thermal effects on a NASP-like body panel in a hypersonic flow. The reports [31,63] involved the insertion of rigid, three-dimensional geometries into hypersonic flows of methane–air combustion products to measure the thermal and structural loads on the models. The motivation for the studies came from the interest in using lightweight, flexible, metallic body panels in lieu of heavy, ablative thermal protection system panels. In the presence of high surface temperatures, flexible body panels bow into the flow field due to through-thickness thermal gradients. The rigid, domed protuberance [31] and quilted dome model [63] represented the deformed geometry of such thermally bowed panels. In both reports, surface temperature, surface pressure, and heat flux data were taken. In a regime in which experimental data are scarce, this series of tests serves as an excellent resource for the validation of the fluid–thermal multiphysics code described previously.

A. NASA Langley 8-Foot High Temperature Tunnel Facility

To successfully predict the response of a test article during the experiments, the tunnel conditions first need to be understood. The

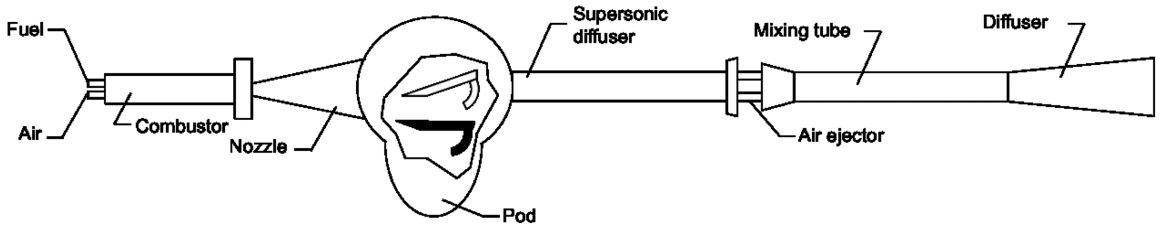

Fig. 3 The Langley 8-Foot High Temperature Tunnel (recreated from Glass and Hunt [63]).

NASA Langley 8-Foot High Temperature Tunnel (8' HTT) (Fig. 3) is a high-energy hypersonic blowdown wind tunnel. Built in the 1960s, it has been used extensively to test various aspects of hypersonic flight vehicles, from thermal protection systems to integrated propulsion systems. The tunnel is capable of simulating aerodynamic heating and pressure loading on test articles in a nominally Mach 7 flow at altitudes of 80,000 to 120,000 ft (24 to 36 km). The high-energy freestream flow is obtained by the combustion of methane and air under pressure in a combustion chamber:

$$\mathrm{CH_4} + 2(\mathrm{O_2} + 3.76\mathrm{N_2}) + \mathrm{Ar} \rightarrow \mathrm{CO_2} + 2\mathrm{H_2O} + 7.52\mathrm{N_2} + \mathrm{Ar} \tag{8}$$

The combustion products are then accelerated to Mach 7 through a conical nozzle terminated by a constant 8-ft diameter section before entering the test section. The attainable freestream dynamic pressures are within the range of 250 to 1800 psi (1.7 to 12.4 MPa), while the total temperatures range from 2400 to 3600 R (1300 to 2000 K). The freestream Reynolds numbers range from 0.3 to 2.2×10^6/ft (1.0 to 7.2×10^6/m), and the tunnel can sustain these conditions for 120 s.

1. *Mechanical Systems*

The test article (e.g., flat plate, spherical protuberance, quilted dome panel) is installed in a cavity of a ceramic flat plate. Initially hidden in a pod below the wind tunnel during startup, the assembly is inserted into the flow in approximately 1.5 s using an elevator with a curved strut model pitch system capable of positioning the test article at an angle of attack of $\pm 20°$ [64]. An angle of attack of 5° was used in the experiments of interest.

2. *Flow Conditions*

The flow conditions for runs 1 and 14 in the 1986 experiment are given in Table 2 of Glass and Hunt [31] and are reproduced in Table 1 of the present paper. The tabulated values were not measured directly by Glass and Hunt [31], but were based on data from previous tunnel surveys. It is noted that the total to static temperature and pressure ratios are those for a thermally perfect gas. Special considerations regarding this fact are discussed next. The freestream properties are dictated by the equivalence ratio of the fuel to oxidizer in the combustor given as

$$\phi = \frac{(n_{\mathrm{CH_4}}/n_{\mathrm{O_2}})_{\mathrm{actual}}}{(n_{\mathrm{CH_4}}/n_{\mathrm{O_2}})_{\mathrm{stoichiometric}}} \tag{9}$$

The equivalence ratios in the combustor were not provided by Glass and Hunt [31].

3. *8-Foot High Temperature Tunnel Flow Conditions*

To accurately model the flow conditions in the 8' HTT, the gas properties of the methane–air combustion products had to be calculated. However, to obtain the needed thermal storage coefficients [specific heat capacities $C_p(T)$ and $C_v(T)$] and transport coefficients [viscosity $\mu(T)$ and thermal conductivity $k(T)$], the composition, and therefore, the equivalence ratio of methane and air, had to be obtained. Leyhe and Howell [46] provide empirical data for the specific heats and curves for viscosity and conductivity corresponding to four equivalence ratios: $\phi = 0.7$, $\phi = 0.8$, $\phi = 0.9$, and $\phi = 1.0$. As mentioned previously, the equivalence ratios for the wind tunnel runs were not given in the Glass and Hunt report [31] and were determined iteratively as follows. First, one of the four ϕ values listed previously was selected. Then, given the total temperature and reactant equivalence ratio, a constant pressure combustion calculation using STANJAN [65] was performed to determine the mole fractions of the products in the freestream. Given the mole fractions of the combustion products and the information given on page 26 of Leyhe and Howell [46], a piecewise polynomial for $C_p(T)$ was constructed from the weighted sum of $C_p(T)$ polynomials for all individual species. The freestream ratio of specific heats γ_∞, total temperature T_0, and total pressure p_0 were then calculated according to

$$\gamma_\infty = \frac{C_p(T_\infty)}{C_p(T_\infty) - R} \tag{10a}$$

$$\int_0^{T_0} C_p(T)\,\mathrm{d}T = \int_0^{T_\infty} C_p(T)\,\mathrm{d}T + \frac{\gamma_\infty R T_\infty M_\infty^2}{2} \tag{10b}$$

$$p_0 = p_\infty \left[\int_{T_\infty}^{T_0} \frac{C_p(T)}{RT}\,\mathrm{d}T \right] \tag{10c}$$

It was found that an equivalence ratio of $\phi = 0.7$ gave the freestream conditions closest to those presented for the runs in Table 1. The curves for $\mu(T)$ and $k(T)$ were digitized from Figs. 14d and 16d on pages 87 and 95 of Leyhe and Howell [46], respectively, and approximated by piecewise polynomials. The representation of the transport coefficient data for the methane–air mixture with polynomials led to errors under 2 and 5% in the $\mu(T)$ and $k(T)$ curve fits, respectively. Additionally, the total temperatures and pressures are reported [66] to vary up to 9 and 20% in the horizontal and vertical extremes of a 4 by 4-ft box centered at the centerline 18 in. downstream of the nozzle exit. These deviations are attributed to condensation in the expansion section. Note that the test article's area of interest sits within the core flow where the experimental variability

Table 1 Experimental conditions of the 1986 tests [31] (run 1 did not include a dome model)

Run	M	$T_{0,\infty}$, K	$p_{0,\infty}$, kPa	p_∞, kPa	D^a, m	H^b, mm	δ^{99}, mm	Materials	Instrumentation	Boundary layer condition
1	6.55	1872	2961	0.655	N/A	N/A	12.7	Ceramic	Pitot probe	Laminar
14	6.59	1894	2896	0.648	0.71	19.3	12.7[c]	Aluminum and ceramic	Thermocouple	Laminar

[a]Dome diameter.
[b]Dome height.
[c]Boundary layer profile only measured at dome location in run 1; expected to be the same in run 14.

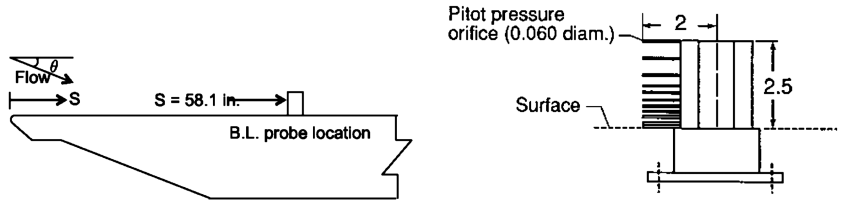

a) b)

Fig. 4 a) Flat plate panel holder and b) boundary layer probe schematic. Units are in inches (taken from Glass and Hunt [63]).

is less, on the order of 5%, and is away from the more highly variable flow closer to the tunnel walls.

4. Verification of the Laminar Boundary Layer

Runs 1 through 15 of the 1986 experiment [31] involved studying the loads on the spherical dome protuberance due to the presence of a laminar boundary layer in hypersonic flow. The laminar boundary layer was produced over the inclined flat panel with a 3/8-in. radius blunt leading edge (Fig. 4a). The laminar state of the boundary layer was verified by comparison with an analytically determined boundary layer profile [67]. The experimental boundary layer profile was measured using a boundary layer probe, as shown in Fig. 4b.

The use of the boundary layer probe is an invasive measurement. The presence of the probe causes a local bow shock, shown in Fig. 5, such that the stagnation pressure measured by the pitot tube is that associated with the postshock flow. To calculate the preshock Mach number, Glass and Hunt [63] used the Rayleigh pitot formula:

$$\frac{p_{t2}}{p_{fp}} = \left[\frac{(\gamma+1)^2 M_1^2}{4\gamma M_1^2 - 2(\gamma-1)}\right]^{\frac{\gamma}{\gamma-1}} \frac{(1-\gamma)+2\gamma M_1^2}{\gamma+1} \tag{11}$$

which relates the total pressure after the shock (p_{t2}) to the static pressure before the shock (p_{fp}). In supersonic applications, measuring the static pressure upstream of the probe is usually done by placing a static pressure probe flush with the wind tunnel wall in a smooth region of the flow. Glass and Hunt [63] did not use a flat plate pressure that they measured during run time at the location of the probe; instead, a reference flat plate pressure from a previous report [31] at a location downstream of the boundary layer probe was used.

B. Initial and Boundary Conditions

To produce the inflow boundary conditions for the coupled simulation domain, a two-dimensional simulation was run using the commercial software, ANSYS Fluent. The solution of this two-dimensional problem was sufficient to provide the inflow boundary conditions because the geometry up to that point was invariant in the third dimension and edge effects were not capable of affecting the region of interest. The two-dimensional simulation also served to validate that the selection of gas properties was consistent with the Glass and Hunt experiment [31]. The two-dimensional Fluent domain was refined until the solution was determined to be grid independent. It is compared with the coupled simulation fluid domain in Fig. 6. The simulation was run on the two-dimensional Fluent domain using the freestream parameters given in Table 1 and gas properties consistent with a combustion chamber equivalence ratio of $\phi = 0.7$. The plate had been heated an unknown amount when the boundary layer measurement was taken. It was assumed that the thermal state of the plate was close to its initial isothermal 300 K condition, and that was the value assigned to the plate in the simulation. The results in Fig. 7 were postprocessed following the procedure used by Glass and Hunt [63] to extract the boundary layer profile. Although the geometry of the probe was not modeled, its presence was simulated by solving for the postshock flow given the unprocessed simulation data. The postshock pitot pressure p_{t2}, the reference flat plate pressure [63] p_{fp}, and the ratio of specific heats [63] $\gamma = 1.38$ were used to solve for the preshock Mach number in the Rayleigh pitot formula [Eq. (11)].

It can be seen in Fig. 7 that the predicted and experimentally measured profiles are similar throughout the boundary layer. The simulation slightly underpredicts the Mach number in the entropy layer. The Mach number in this region is very sensitive to the leading edge geometry and boundary conditions, for which the data are not available to be fully confident that the experimental setup was

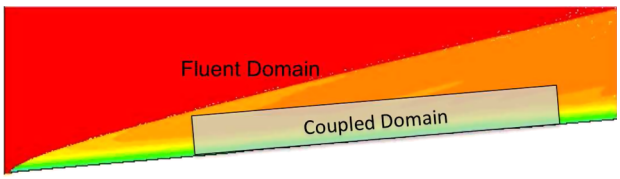

Fig. 6 Two-dimensional Fluent domain with Mach number contours. The coupled simulation uses the Fluent solution to provide boundary conditions and an initial guess for the solution.

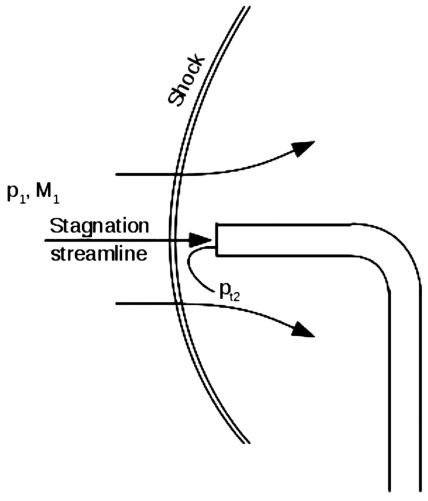

Fig. 5 Pitot probe in supersonic flow.

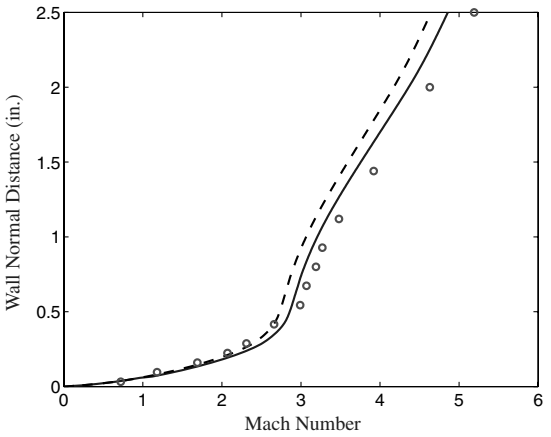

Fig. 7 Boundary layer profile at $X = 1.476$ m. Simulation data processed with Eq. (11) (solid), unprocessed simulation data (dashed), and experiment (circles) [31].

represented exactly. The agreement between the simulation and experiment is sufficiently accurate to validate our assessment of the tunnel flow and gas properties.

C. Insertion Procedure

In the 8' HTT, test articles were inserted into the initialized hypersonic freestream over a period of 1.5 s; before this time, they were held below and outside the established freestream. Heating of the panel by the flow occurred during the panel insertion from an angle of attack of 0° to an angle of attack of 5°. To accurately model the temperature distribution in the thermal domain at the moment that it reached the 5° position, a fully coupled, transient simulation of the panel insertion would have to be done. A simulated one-dimensional panel insertion was done to estimate the amount of heating that would take place during the insertion time and evaluate the best course of action. The heating of a one-dimensional rod was modeled using a transient finite element code developed in MATLAB. The material properties, boundary conditions, and geometry of the rod were chosen to be consistent with the aluminum sheet metal heat flux dome in run 14 of Glass and Hunt [31]. To provide the heat flux from the fluid, the compressible self-similar boundary layer equations were solved. The parameters for the flow were chosen to be the postoblique shock flow conditions consistent with the Glass and Hunt scenario [31] at a location similar to that of the heat flux dome. The coupling setup can be seen in Fig. 8. The 1.5 s were divided into discrete time steps, and at each time step, the angle of the flat plate was incremented toward 5°. At each increment, the postoblique shock conditions were calculated and passed along with the plate surface temperature to the boundary layer code to solve. The surface heat flux was taken from the solution of the boundary layer equations and provided as a thermal load on the coupled boundary of the one-dimensional thermal domain. The thermal domain was then integrated one time step and returned a new surface temperature as a boundary condition to the fluid domain. This process was iterated until the heat flux and wall temperature were converged. At the end of the 1.5-s insertion time, with the final angle of attack of 5° attained, the surface temperature at the location of the heat flux dome was estimated to have risen 2 K from the initial temperature of 300 K. This temperature rise was determined to have a negligible effect on the heat flux, and therefore, the initial condition of the coupled simulation could be taken as a 300-K isothermal wall boundary condition to the fluid domain and a uniform temperature in the thermal domain.

D. Coupled Fluid–Thermal Simulation

The experiment featured in the 1986 report [31] was selected to be the validation case for the fluid–thermal solver. Of the 33 experimental configurations investigated in the report, run 14 was selected for the present simulation. This particular run featured a single aluminum dome installed in a ceramic flat plate. The 28.6-mm-thick flat plate was made from Resco Cast RS-17E refractory ceramic. The aluminum dome was made from 14 gauge sheet metal (1.57 mm thick). The spherical dome had a 3.28-m radius of curvature and a diameter of 0.71 m. The backside of the dome was exposed to an evacuated chamber. Material properties are listed in Table 2. The assembly was inserted into a Mach 6.59 freestream as described in the prior section. Details of the experiment are given in Table 1.

Table 2 Material properties in thermal domain

Material	Density ρ, kg/m^3	Conductivity k, W/m · K	Specific heat capacity C_p, J/kg · K
Resco RS-17EC	2192	1.07	750
Aluminum (7000 series)	2800	155.0	883

1. Fluid and Thermal Domains

For the coupled simulation, the fluid domain is discretized with a single 288 × 313 × 97 structured grid, totaling more than 8.7 million grid points. The grid is designed to have an estimated y^+ value less than 5 for the first wall normal grid point to guide the near-wall resolution. It is confirmed by simulation results (Fig. 9) that the y^+ value is less than 2 everywhere in the domain. In a later section, a grid convergence study shows this wall normal refinement to be sufficient. The surface grid extends away from the wall with a geometric growth rate less than 1%. Fluid grid convergence data are given later in this section.

The thermal domain is meshed with 878,000 linear 8-node brick finite elements and is modeled to represent closely the dome geometry described in the 1986 report. As mentioned perviously, the domain is made up of two parts with different material properties that have to be meshed separately with matching nodes along the material interface. The ceramic flat plate portion has a high mesh density near the surface to capture the thermal gradients at the fluid–structure interface, but then is stretched into the plate. The aluminum dome is meshed with 10 elements through its thickness. This mesh density is shown to produce spatially invariant results for an analogous one-dimensional finite element solution for the present conditions. The spatial resolution of the thermal domain is discussed further in Sec. IV.F. The dome is backed by an evacuated chamber, represented by an adiabatic boundary condition.

Figure 10 shows the orientation and boundary conditions of the two domains. The boundary conditions on the thermal domain are set to adiabatic everywhere except on the interacting surface. The initial condition in the thermal domain is a uniform temperature of 300 K. In the fluid, a symmetry plane bisects the dome while the other spanwise boundary is modeled as a slip wall because edge effects from the

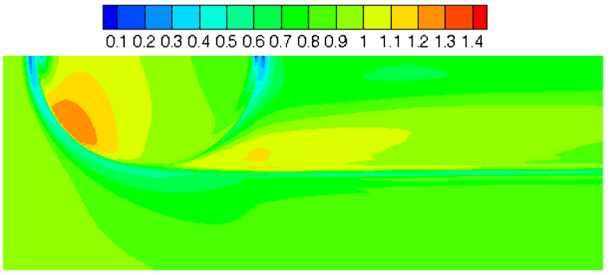

Fig. 9 y^+ values of the first wall normal grid point at $t = 0$ s.

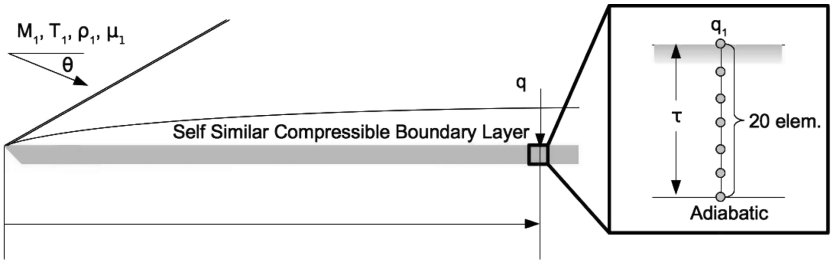

Fig. 8 One-dimensional fluid–thermal problem to estimate insertion heating. The rise in surface temperature during model insertion was estimated to be 2 K.

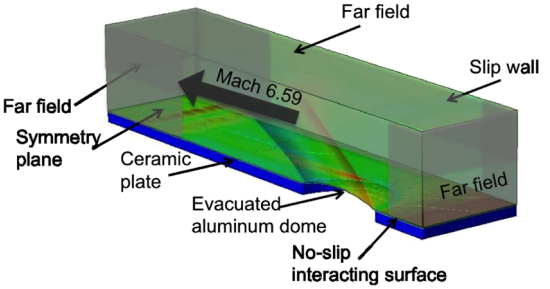

Fig. 10 Boundary conditions of the fluid and thermal domains. Shaded regions represent sponges.

panel holder do not influence the region of interest. The inflow, top, and outflow are treated as far field boundaries. The reference solution for the far field boundaries is provided by a target solution generated by an ANSYS Fluent simulation of the complete panel at a 5° incline in the Mach 6.59 freestream flow (Fig. 6). The target solution for this simulation is a composite consisting of a refined two-dimensional Fluent solution over the full domain and a coarse three-dimensional Fluent simulation of the full domain. The inflow region is dominated by the two-dimensional solution to provide an accurate and inexpensive estimate for the inflow conditions, while the three-dimensional solution is used in the region above and aft of the dome to provide a reasonable match between a three-dimensional varying internal solution and the fixed boundary conditions. The shaded regions in Fig. 10 represent sponges that blend the target solution with the internal solution to promote simulation stability near the boundaries. The target solution also provides a fair initial condition in the fluid domain, which reduces overall the simulation time. All reported results do not include data from the sponge-influenced regions.

2. *Fluid Steady-State Convergence*

As mentioned previously, the temporal coupling is done in a quasi-static configuration, in which the transient-thermal problem is solved given the heat flux from the steady-state fluid solution at each thermal time step. In a previous paper [68], we considered several definitions of fluid steady state and found that, for the quantity of interest (heat flux into the thermal domain), the change between fluid iterations in the root mean square (rms) of the heat flux over the interacting surface

$$\Delta q_{\text{rms}} = \frac{\sqrt{\sum_{i=1}^{N}(q_{i,k+1} - q_{i,k})^2}}{N}$$

was an appropriate metric. Further, through a convergence study, it was concluded that a criterion of $\Delta q_{\text{rms}} < 1 \times 10^{-3}$ W/m^2 was sufficient to provide accurate results.

3. *Fluid Spatial Convergence*

The primary goal of this study is to simulate the heat flux into the aluminum spherical dome protuberance in the Mach 6.59 flow, for which experimental data are available. To be sure that the predicted heat flux is an accurate solution of the Navier–Stokes equations, grid independence must be verified for the solution on the spherical dome. As the heat flux into the surface is most sensitive to the wall normal resolution of the solution, the grid is designed to be very fine at the wall. A fluid-only simulation confirms that the y^+ value has a maximum value of approximately 1.1 on the dome surface. To ensure that this is sufficient, a homothetic grid refinement by a factor of 2 in the wall normal direction is done, resulting in a $288 \times 625 \times 97$, 17.4 million–point grid. The solution, after being run to steady state as defined previously, is compared with the solution from the original grid. The maximum y^+ value for the new grid is less than 0.6, and occurs on the flat plate next to the dome. The heat flux into the dome differs from the original results by less than 0.1%. The small difference suggests that the grid point distribution in the wall normal direction in the original grid is fine enough to capture the heat flux into the dome.

To ensure grid independence in the streamwise and spanwise directions, the original, 8.7 million–point grid is refined homothetically by a factor of 2 along both directions simultaneously, resulting in a $575 \times 313 \times 193$, 34.7 million–point grid. The resulting steady-state heat flux is again compared with that from the original grid. The change in heat flux on the dome is less than 0.3%, indicating that the 8.7 million–point grid is suitable for the coupled fluid–thermal simulation for prediction of heat flux into the dome. However, this refinement shows that the grid requirements off the dome are more stringent than those on the dome. Further refinement is done for a fluid-only investigation into the flow features in these regions. The solution on the finest grid is discussed in Sec. IV.D.

IV. Results

A. Effect of Numerics on Surface Heat Flux

As mentioned in Sec. II.A, the viscous terms of the Navier–Stokes equations are evaluated in the present work using the strong form due to its computational efficiency. For stability reasons, the strong form requires the use of solution filtering to provide numerical damping. Preliminary simulation results indicate that the heat flux calculated at the surface is very sensitive to the level of filtering used. Several small, two-dimensional, fluid-only simulations are run over a flat plate under the same freestream conditions to understand and avoid the inaccuracies introduced by the filter. The two-dimensional simulations are run on a grid similar to that used in the coupled simulation of the Glass and Hunt case (Sec. III.D.1), and extended over the region forward of the dome. The two-dimensional initial and boundary conditions from the Glass and Hunt simulation are used to make the results relevant to the three-dimensional simulation. The two filter parameters that affect the solution are the filter strength (α_f) and whether the filter uses biased, high-accuracy stencils as the boundary is approached or centered stencils but with decreasing stencil size and order. Unfiltered solutions using the Cartesian and weak form (not shown) of the viscous terms converge to the same values. In the strong form simulations using the centered filter, the heat flux very slowly converges to the values found by the unfiltered Cartesian form, significantly underpredicting the heat flux, as shown in Fig. 11a. When using the boundary filter, the strong form predictions converge to those of the unfiltered Cartesian form (Fig. 11b) and were thus used for all simulations in this work. Figure 12 shows that the centered filter affects the heat flux by modifying the temperature profile in the boundary. The shallower temperature gradient directly affects the heat flux into the plate. Temperature differences at several wall normal locations are noted for clarity.

B. Assessment of Gas Thermal Model

With the uncertainties associated with the grid and numerics quantified, results are presented from the coupled fluid–thermal simulation of a Mach 6.59 flow over a flat plate with a spherical protuberance. The fluid–thermal solution is advanced to 5 s in time in accordance with run 14 of the 1986 Glass and Hunt experiment [31]. The regions of interest are the dome surface and surrounding areas. Results for longer run times are given later in this paper.

As mentioned earlier, the flow solver has the capability of simulating a calorically perfect or thermally perfect gas. It can be seen in Fig. 13a that the ratios of specific heats ($\gamma = C_p/C_v$) of these two models diverge from each other at higher temperatures. Coupled fluid–thermal simulations are run to 5 s using each of the gas thermal models to assess the differences in the resulting heat fluxes and thermal (solid) solution. Referring to Table 1, the temperature data given in Glass and Hunt [31] are the total temperature based on the 8' HTT combustor conditions. The total temperature and freestream Mach number are used to calculate the freestream static temperature for the inflow boundary condition of the coupled simulations. To be consistent, the calculation of the freestream temperature is calculated by $T_\infty = T_{T,\infty}(1 + [(\gamma - 1)/2]M_\infty^2)^{-1}$ in the calorically perfect case, and Eqs. (10a) and (10b) in the thermally perfect case. The

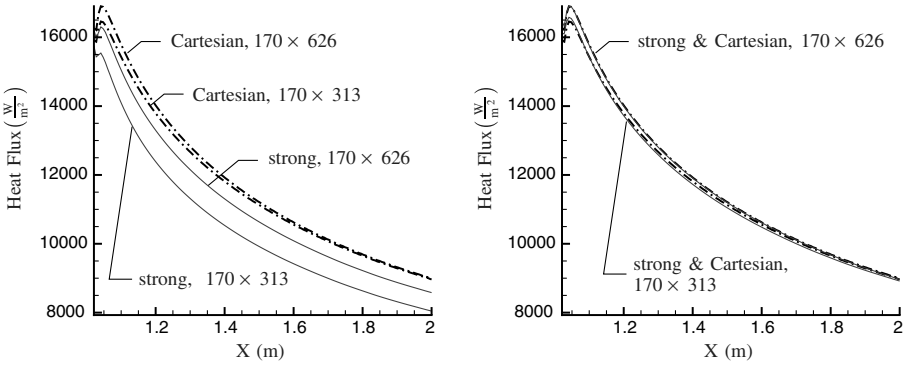

Fig. 11 Effect of spatial filter on convergence of surface heat flux: a) centered filter, and b) boundary filter. Cartesian (dashed) and filtered strong form viscous terms (solid).

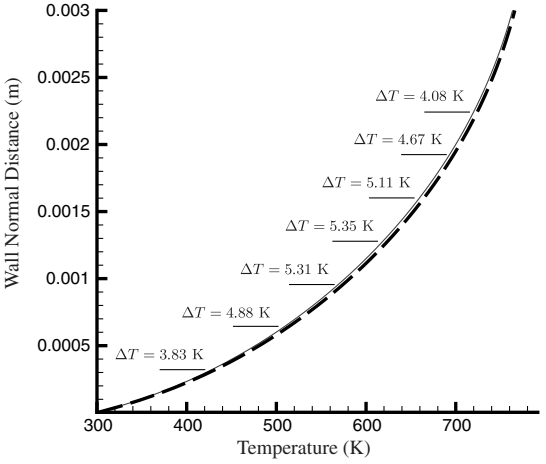

Fig. 12 Temperature profiles in the boundary layer at $X = 1.58$ m. Centered filter (solid) and boundary filter (dashed) on the finer grid (170 x 626).

resulting freestream temperatures are 204.73 and 237.14 K in the calorically and thermally perfect cases, respectively.

Figure 14a shows heat flux along the symmetry plane of the dome from the fluid–thermal coupled simulations using both the calorically and thermally perfect gas models. The thermally perfect model consistently predicts higher heat flux values into the dome and flat plate. Interestingly, the variation in heat flux over time is seen to be less in the thermally perfect case. This is due to the increase in C_v with temperature (Fig. 13a), as given by $C_v = R/(\gamma - 1)$. The boundary layer thickness increases less with temperature as C_v increases, which results in the wall normal temperature gradient being less sensitive to the surface temperature. Therefore, the heat flux decreases less in the thermally perfect case. The resulting surface temperature as the fluid–thermal coupled simulation progresses from 1 to 5 s is shown in Fig. 14b. As expected from the heat fluxes, the temperature along the symmetry line is also consistently higher in the thermally perfect case. Although the total temperature of the gas in the two simulations is the same, the total energy in the calorically perfect case is less than that in the thermally perfect case. This is because at $T_{T,\infty} = 1894$ K, the specific heat capacity is higher in the thermally perfect case. When compared with the heat fluxes reported by Glass and Hunt [31], the values from the thermally perfect simulation are closer than those from the calorically perfect simulation. Unless otherwise stated, all further results represent the thermally perfect gas model. A comparison between solutions from the two models when using identical static freestream conditions is presented in the Appendix.

C. Surface Temperature Evolution

Figures 15a–15c show the evolution of the surface temperature at three times during the 5-s coupled simulation. The surface temperature contours give insight into the flow physics. As the time progresses, the largest temperature increase occurs in two regions. Although the whole front half of the dome shows an obvious temperature increase, the forward-most portion of the dome exhibits the most elevated temperature. The increased heat flux in this region is due to the flow impinging on the front of the dome. A second region of large temperature increase is located just past the outer spanwise extreme of the dome on the ceramic plate. This is a viscous effect generated by the impingement of vorticity shed off of the dome. Interestingly, the surface temperature in this region is slightly higher than that at the flow impingement region, while Fig. 16 shows a larger heat flux at the front of the dome. This is a function of the thermal properties of the dome (aluminum) and flat plate (ceramic), and will

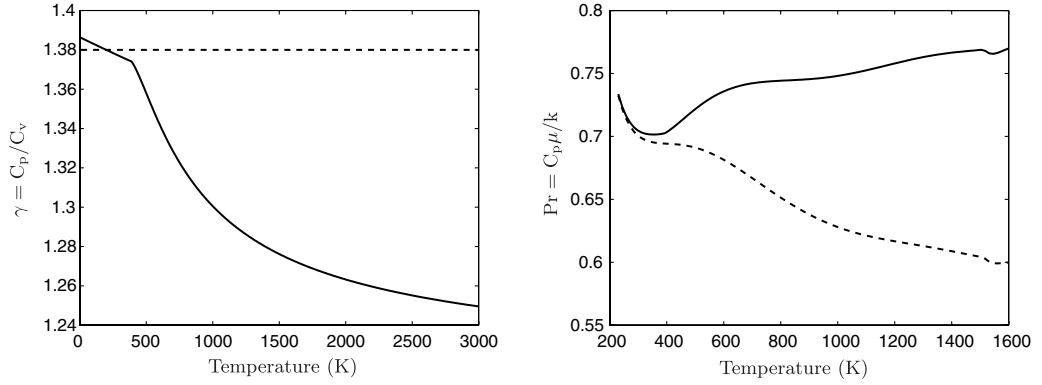

Fig. 13 Variation in a) ratio of specific heats and b) Prandtl number with temperature [calorically perfect (dashed line) and thermally perfect (solid line)].

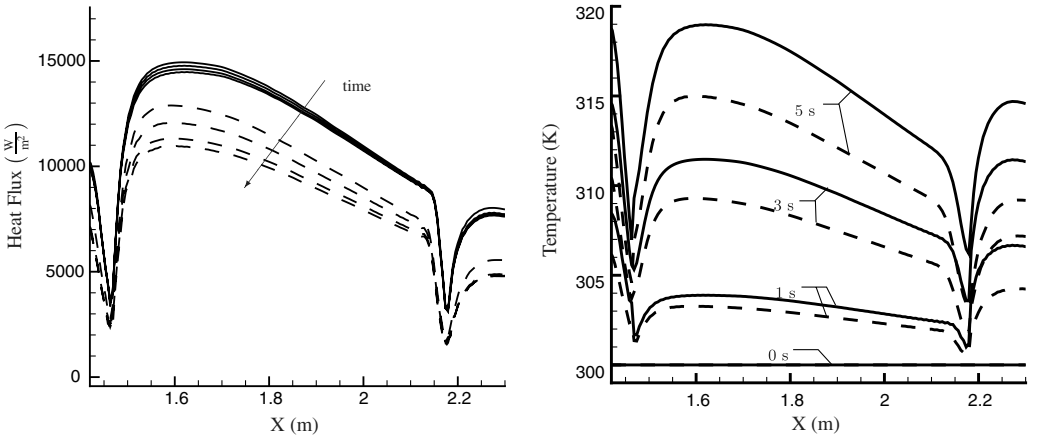

Fig. 14 a) Heat flux and b) temperature profiles at the symmetry line at $t = 0$ s, $t = 1$ s, $t = 3$ s, and $t = 5$ s. Calorically (dashed) and thermally perfect (solid) gas models.

be addressed in Sec. IV.E. Another phenomenon, most apparent in Figs. 15c and 16, is the occurrence of low heat flux regions along the circumference of the dome. The close proximity of high and low heat flux indicates that there is an extreme change in the behavior of the flow in these regions.

D. Flow Solution Features

Investigation of the flow behavior at time $t = 0$ s at the surface provides information about the mechanisms that lead to the thermal features discussed in the previous section. Figures 17a and 17b show the surface streamlines, as visualized through the surface shear stresses, along with heat flux and pressure contours, respectively. The shear stress visualization in Fig. 17a shows that there is a correlation between the flow separation and recirculation and the regions of low heat flux. Figure 17b shows the relation between the recirculation regions and the pressure gradients.

To investigate the flow features responsible for the high and low surface temperatures that develop on the flat plate in Fig. 15, the $575 \times 313 \times 193$ grid is again refined by a factor of 2 in the spanwise direction, producing a $575 \times 313 \times 385$ grid with just under 69.3 million grid points. Although the original grid is fine enough to resolve the solution on the dome, surrounding areas on the flat plate are subject to more complex three-dimensionally varying flows and require a denser grid in the surface tangent directions. It can be clearly seen in Fig. 18 that both the region of increased heat flux behind the dome and the long, low heat flux strip are both related to a vortex shed off the dome. The vortex creates the low heat flux strip by lifting the cool gas from the plate surface, decreasing the wall normal temperature gradient. Simultaneously, the vortex forces hot gas from within the boundary layer (refer to Fig. A1b) to the plate surface, resulting in the high heat flux region aft of the outer side of the dome. A slice of the X-vorticity to the outside of the dome (Fig. 19) exposes a counter-rotating vortex pair above the low heat flux strip. As mentioned previously, the strong negative vorticity structure is primarily responsible for convecting the hot boundary layer gases to the plate surface.

A common method for calculating heat transfer is by its relation to the wall shear stress through a Reynolds analogy. In the Reynolds analogy for compressible flows

$$\frac{C_h}{C_f} = \frac{q_w U_\infty}{2C_p \Delta T \tau_w} = \frac{Pr^{-2/3}}{2} = 0.62$$

C_f is the friction coefficient and C_h is the Stanton number. The temperature difference is calculated as $\Delta T = T_{\text{aw}} - T_w$, where the compressible adiabatic wall temperature is given by

$$T_{\text{aw}} = T_\infty + r(Pr)\frac{U_\infty^2}{2C_p}, \qquad r(Pr = 0.727) = 0.8519$$

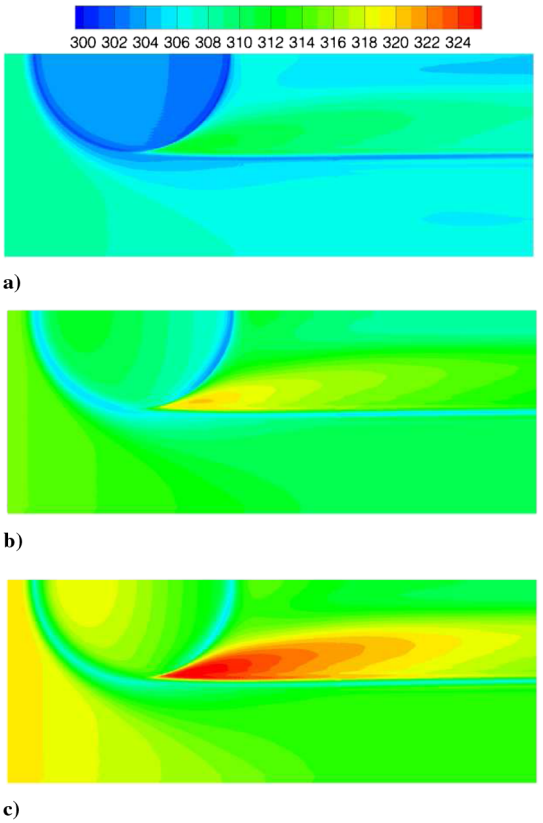

Fig. 15 Surface temperature, K, at a) $t = 1$ s, b) $t = 3$ s, and c) $t = 5$ s.

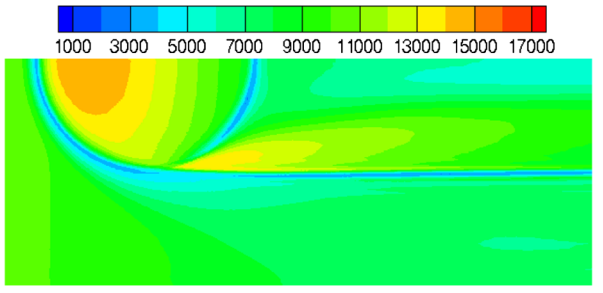

Fig. 16 Surface heat flux, W/m^2, at $t = 1$ s.

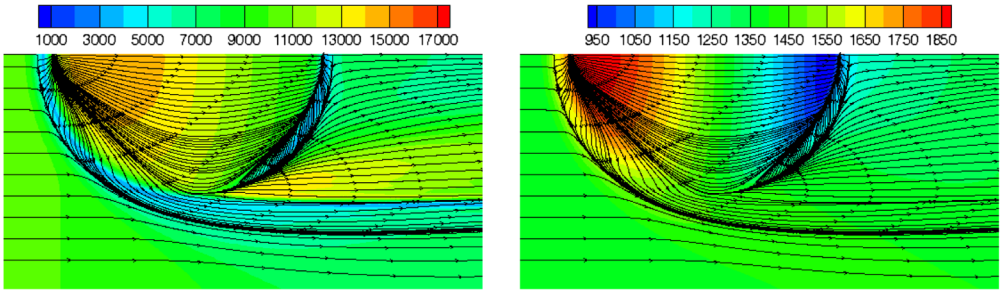

Fig. 17 Shear stress vectors with a) heat flux (W/m^2) and b) pressure contours (Pa).

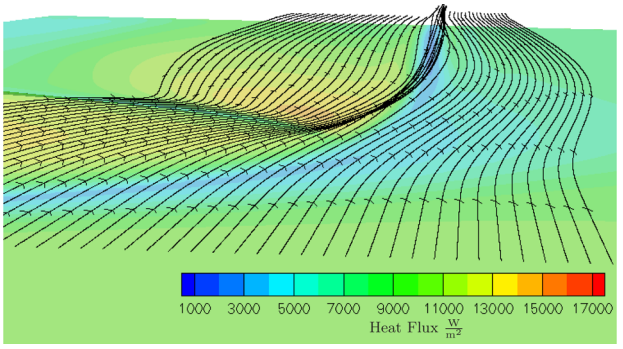

Fig. 18 Streamlines illustrating a vortex shed off the right side of the dome. Heat flux contours are shown on the thermal domain surface.

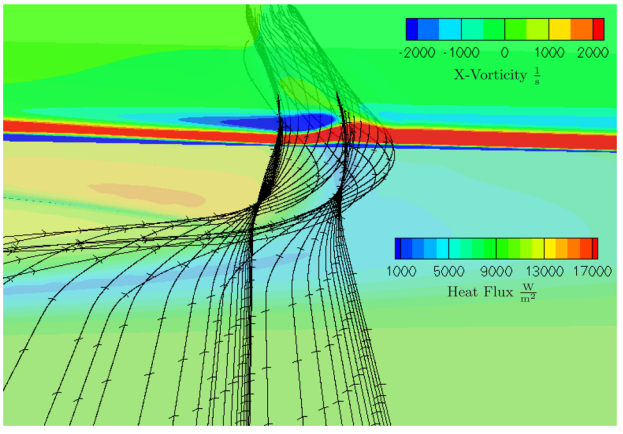

Fig. 19 Counter-rotating vortex pair grazing the plate on side of the dome. Surface heat flux and vertical plane x-vorticity contours shown.

The Prandtl number for the combustion products of methane and air in the present study is $Pr = 0.727$ in the freestream. The quotient C_h/C_f is calculated from the simulation data to test the validity of the Reynolds analogy over a varying geometry. Figure 20 shows that the Reynolds analogy predictions are low (20% lower than simulation results), but otherwise reasonably estimate the heat flux into the flat plate. However, the analogy breaks down near the compression regions at the front and back of the dome, where it grossly underestimates the heat flux. It is known that, in compressible flows with pressure gradients, the Reynolds analogy is less useful, a fact reflected in Fig. 20. Additionally, in flows involving large temperature ranges, this model may be inadequate due to its assumption of a constant Prandtl number. For both the thermally perfect and calorically perfect gas models used in this simulation, the Prandtl number varies significantly over the temperatures present in the flow field (Fig. 13b). Note that Pr is not constant for the calorically perfect model because of the temperature variation of the methane–air μ and k properties.

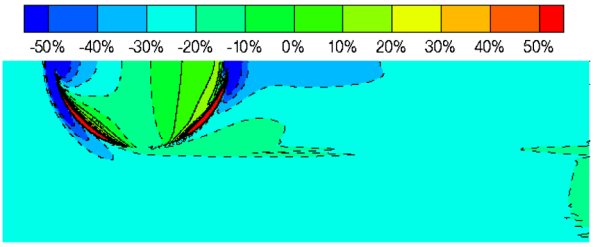

Fig. 20 Percent difference between value predicted by Reynolds analogy (0.62) and C_h/C_f calculated over the interacting surface at $t = 0$ s. $\%\text{difference} = \frac{0.62 - C_h/C_f}{C_h/C_f} \times 100\%$.

E. Thermal Solution

Figures 21a–21c and 22a–22c show the temperature distribution in the thermal domain at three different times during the simulation. It is noted in Sec. IV.C that the surface temperature at the region aft of the dome is higher than that on the the windward face of the dome where the heat flux is higher. The through-thickness thermal solution reveals that the surface temperature on the flat, ceramic portion of the model is very high in regions, but the temperature quickly decreases with distance into the material. This is very different from the temperature distribution in the aluminum part of the model, where the temperature is lower but nearly constant through the thickness. The reason for this is the large difference in the thermal diffusivities, $\kappa = k/\rho C_p$, of the two materials (aluminum: $\kappa = 6.65 \times 10^{-5}$ m^2/s, Resco RS-17E refractory ceramic: $\kappa = 6.51 \times 10^{-7}$ m^2/s).

F. Quantitative Comparison with Experiment

In the experiment, the aluminum dome had 58 thermocouples soldered to the backside of it. With the time-varying temperature measurements from the thermocouples, the surface heat flux through the aluminum dome was calculated using

$$q = \rho C_p \tau \frac{\Delta T}{\Delta t} \tag{12}$$

The rate, $\Delta T/\Delta t$, was approximated using a central difference over three data points. This value was calculated and reported for only one instant in time, just after the model reached the tunnel centerline. Equation (12) is based on several assumptions: 1) the through-thickness temperature is constant, 2) the backside of the dome is perfectly insulated, 3) the specific heat capacity is constant, 4) heat conduction is one-dimensional, and 5) the thickness of the dome is constant. The temperature contours in Figs. 22a–22c and the fact that the backside of the dome is evacuated suggest that the first two assumptions are valid. The third and fifth assumptions will be revisited at the end of the section.

To compare quantitatively the simulation thermal response predictions with the experimental results, the temperatures over the 5-s run at 13 of the 58 locations are monitored. The temperature and time data at these 13 locations are postprocessed using Eq. (12) and normalized by the flat plate reference heat flux for run 14 in the report, $q_{\text{ref}} = 0.669$ Btu/ft^2s (7597 W/m^2). The data are compared at a time shortly after the model insertion, at $t = 0.1$ s, in the

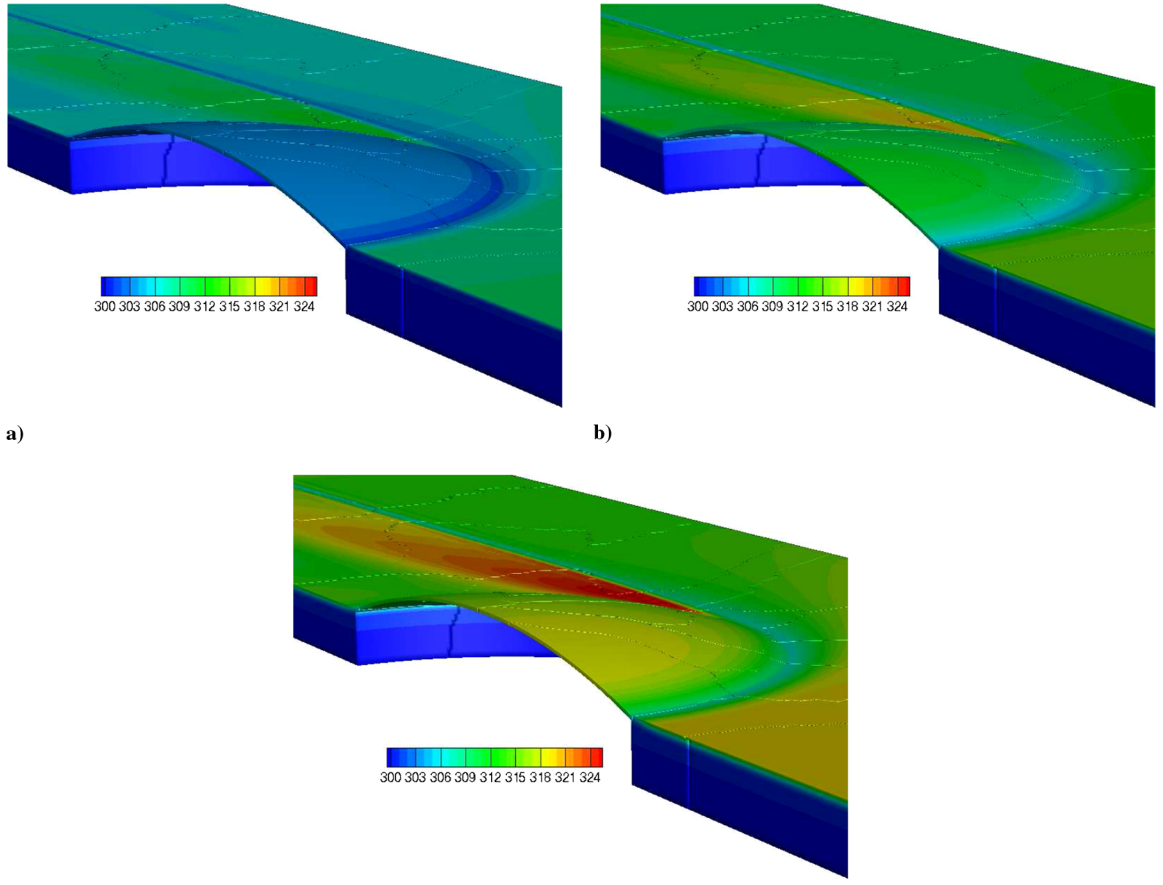

Fig. 21 Evolution of thermal solution on the windward side of dome at a) $t = 1$ s, b) $t = 3$ s, and c) $t = 5$ s. Units are Kelvin.

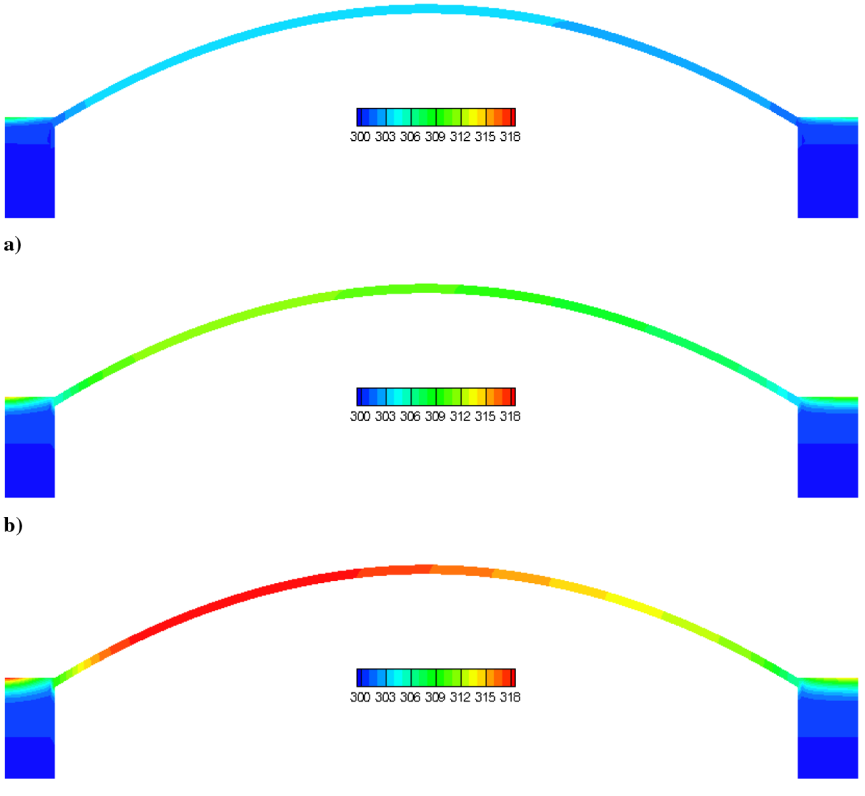

Fig. 22 Evolution of through-thickness dome temperature (K) at the symmetry plane at a) $t = 1$ s, b) $t = 3$ s, and c) $t = 5$ s.

Thermocouple Number	% Diff. Thermally Perfect	% Diff. Calorically Perfect
2	-7.19 %	-20.29 %
3	-0.91 %	-15.65 %
4	+7.47 %	-9.53 %
7	+11.86 %	-8.11 %
10	+11.01 %	-7.52 %
12	-19.40 %	-31.01 %
19	-1.74 %	-18.62 %
21	-18.96 %	-31.97 %
28	+2.33 %	-16.09 %
30	-5.29 %	-23.04 %
37	+1.26 %	-17.55 %
39	+1.54 %	-18.06 %
41	+4.51 %	-15.10 %

a)

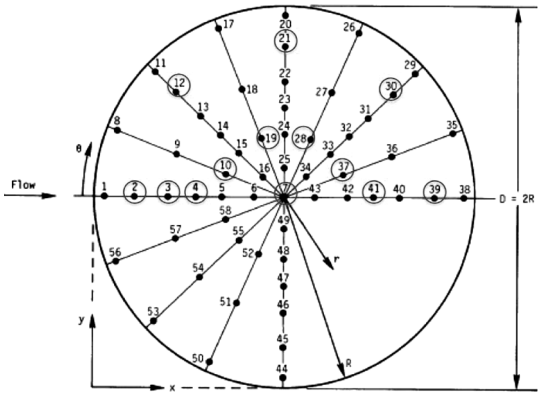

b)

Fig. 23 a) Comparison between experimental and numerical values for heat flux at the 13 thermocouple locations denoted by circles in b). $\%\text{difference} = \frac{q_{\text{sim.}} - q_{\text{exp.}}}{q_{\text{exp.}}} \times 100\%$.

simulation. The results of the comparison shown in Fig. 23 indicate that the thermally perfect gas model clearly performs better than the calorically perfect model. The more rapidly decreasing heat flux in the calorically perfect case (Fig. 14) implies that the underpredictions made with the calorically perfect model would worsen over longer time records. Regarding the thermally perfect model, the simulation and experimental values are within 12% difference at all probes except at 12 and 21, where the heat flux calculated from the temperature probes in the simulation underpredict the heat flux as compared with the experiment. Negative differences of 5% or more are grouped along the periphery of the dome, while positive differences exceeding 5% occur toward the center. This is more easily seen in Fig. 24b. On the edge of the dome, there may be more complicated aspects in the experimental configuration than represented in either Eq. (12) or the computer model. Glass and Hunt [31] note that the aluminum dome is secured to the panel with countersunk screws along the perimeter of the dome, and a maximum gap of 0.03 in. (0.7 mm) between the dome and flat plate also exists. The fasteners would change both the geometry of the dome [possibly invalidating the constant thickness and one-dimensional heat flux assumptions in Eq. (12)] and the local surface topology experienced by the fluid. Also, in the numerical discretization of the thermal domain, the dome/panel interface is modeled to simply be a jump in the material properties. There is no gap or filler material to insulate the dome from the plate. These inconsistencies may contribute to the differences between the numerical and experimental heat flux values near the dome edges.

Glass and Hunt [31] also mention that the assumption made in Eq. (12) of constant specific heat capacity may result in 3–10% underestimates in the heat flux. They reason that, by normalizing with the flat plate reference heat flux (which also would contain the associated errors), the impact is minimized. The minimization would be least effective in regions of higher heat flux (higher temperatures). This would be one possible reason for the overpredictions made by the simulation toward the center of the dome, where the heat flux is elevated. Glass and Hunt [63] also state that the uncertainty in the sheet metal dome thickness varies by ±2%. The dome is

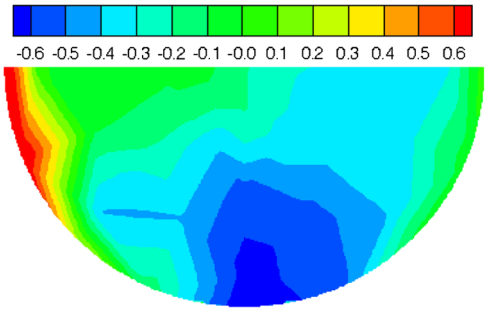

a)

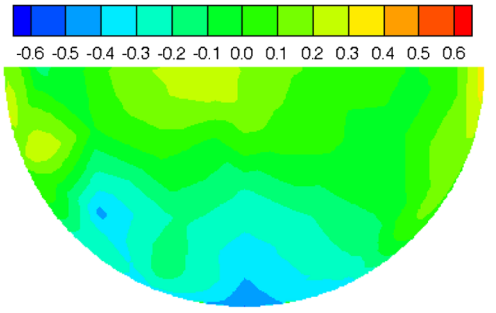

b)

Fig. 24 Comparison between heat flux calculated with a) semi-analytical and b) high-fidelity models ($t = 0$ s). Normalized differences between numerical and experimental heat fluxes shown, $(q_{\text{num.}} - q_{\text{exp}})/q_{\text{ref}}$.

instrumented with K-type chromel–alumel thermocouples, which can introduce an uncertainty of ±2.2% [69]. The combined experimental uncertainties in the heat flux measurements are thus expected to be +4.2% to −14.2%.

The validity of heat flux estimates made with Eq. (12) (without the complications of varying material properties and manufacturing defects) is assessed by comparing these estimates with the true heat flux calculated at the surface of the dome directly from the fluid solution, $q_n = -k\Delta T \cdot \boldsymbol{n}$, where $\boldsymbol{n}$ is the wall normal unit vector. The heat flux values calculated by the two different methods are within 1% of each other, confirming that the assumptions in Eq. (12) and

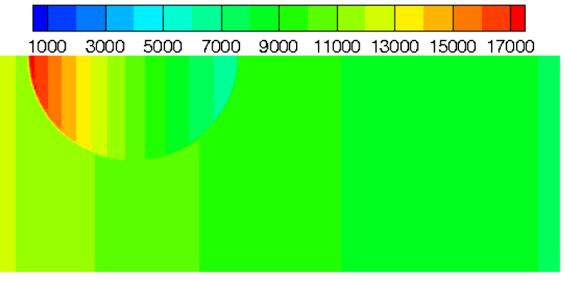

a)

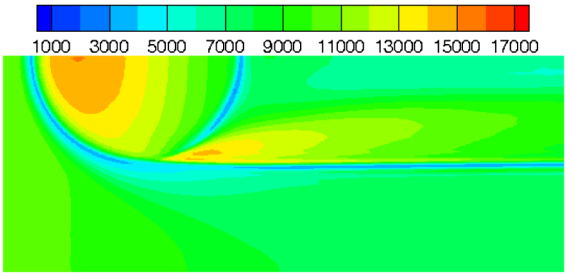

b)

Fig. 25 Comparison between heat flux (W/m^2) calculated with a) piston theory/Eckert's reference temperature and b) the high-fidelity model at $t = 0$ s.

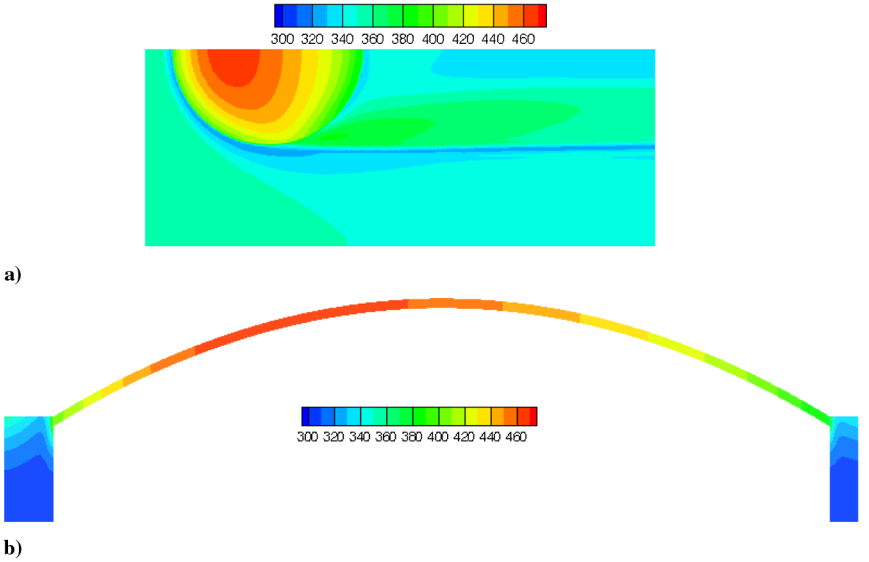

Fig. 26 a) Surface temperature and b) through-thickness dome temperature at the symmetry plane at $t = 50$ s. Units are in Kelvins.

the resulting heat flux values are accurate in the numerical model. It should be noted that this is true for both the center and perimeter temperature probes, indicating that the material property jump model of the dome/plate interface does not significantly affect the temperature distribution in the dome, and may not be a contributing factor to the differences seen in Fig. 23. In addition, the agreement of Eq. (12), which uses data from the thermal solution, with the heat flux calculated directly from the fluid data confirms that the discretization of the thermal domain is sufficient for this problem.

It deserves consideration that thermomechanical deformation of the dome, neglected in the fluid–thermal simulation, may be an additional factor present in the experiment. Such a case would advocate the need for increased coupling (fluid–thermal–structural) to make reliable predictions in hypersonic environments.

G. Comparison with a Semi-Analytical Model

A comparison is made between the heat flux from the high-fidelity model with a commonly used semi-analytical model based on third-order piston theory [19] and Eckert's reference temperature [20]. The method, founded on inviscid aerodynamics, is based on the assumption that the freestream Mach number is large and that surface inclination is small enough so that the surface normal velocity component does not exceed the speed of sound. Further, one of the parameters in Eckert's reference temperature method is the distance from the sharp leading edge of a flat plate. As the leading edge of the geometry under consideration is blunt, an effective sharp leading edge is calculated from the streamwise evolution of the boundary layer thickness from the two-dimensional ANSYS Fluent solution using Eq. (13), where $\boldsymbol{x}_0$ is the distance upstream of the blunt leading edge to the effective sharp leading edge and x is the distance from the blunt leading edge to the δ^{99} measurement location.

$$\delta^{99} = \frac{5(\boldsymbol{x} + \boldsymbol{x}_0)}{\sqrt{Re_{x+x0}}} \tag{13}$$

The effective leading edge is found to be 0.15 m forward of the blunt leading edge. Further details on the piston theory/Eckert's reference temperature approach are given in Culler and McNamara [17].

A comparison between the heat flux at the surface of the model as predicted by the semi-analytical model and the high-fidelity model shows the similarities and differences between the two approaches (Fig. 25). Both methods predict an increased heat flux on the windward face and a decreased heat flux on the leeward face of the dome. However, although qualitative trends in heat loads are similar, a quantitative comparison shows an increased heat load prediction by the simpler approach, with significant features in the heat flux not at all represented.

A comparison of the heat flux over the dome with that measured experimentally by Glass and Hunt [31] (Fig. 24) confirms that the semi-analytical model grossly overpredicts the heat flux on the windward side of the dome while underpredicting on the side and back of the dome. The underprediction can be attributed to viscous effects, such as the fact that the boundary layer is thicker on the rear of the dome, making the surface declination of the effective shape less than that of the actual geometry. The high-fidelity model slightly

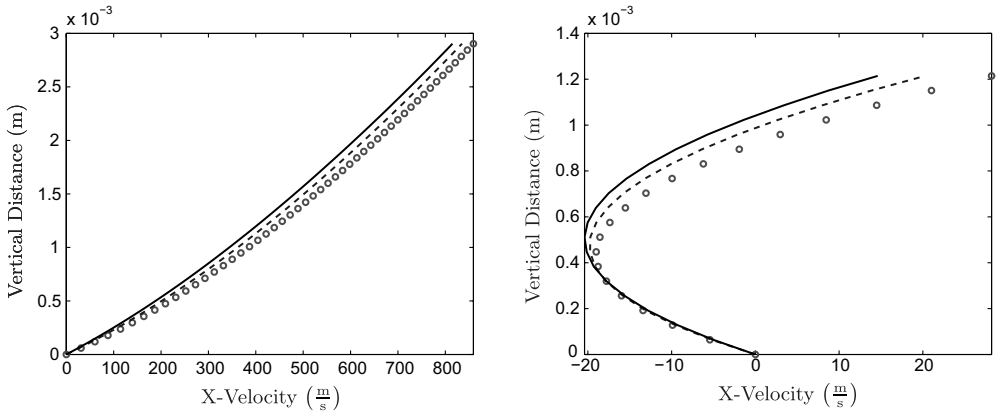

Fig. 27 Boundary layer profile: a) windward face of dome and b) dome leading edge at $t = 10$ s (circles), $t = 30$ s (dashed), and $t = 50$ s (solid).

Table 3 Evolution of drag and integrated heat load with time (drag is calculated assuming both temperature-varying and constant viscosities to demonstrate the effect of boundary layer thickening)

Time, s	Drag, $\mu(T)$, N	Drag, μ = constant, N	Integrated heat load, W
0	14.253	12.632	15,341
10	14.122	11.578	14,388
30	14.102	11.119	13,905
50	14.087	10.821	13,556

overpredicts at the center of the dome and has both positive and negative differences in isolated locations along the perimeter of the dome. It should be noted that, in Figs. 24 and 25, the heat flux is calculated directly from the fluid solution, whereas the values from the experiment were calculated using thermocouples and Eq. (12). In Fig. 24 the heat flux values are normalized by the at plate reference heat flux, q_{ref} [31].

H. Fifty-Second Coupled Simulation

As mentioned earlier, the coupled simulation is continued to a final time of 50 s. Glass and Hunt [31] collected 5 s of quantitative data during run 14. The modest temperature increase over that time is not sufficient to exhibit the advantages gained by two-way fluid–thermal coupling, as the fluid solution is not altered significantly by the surface temperature increase. However, after 50 s, the surface temperature increase is more impressive. As shown in Figs. 26a and 26b, the maximum temperature reaches 465 K and occurs on the windward face of the dome as opposed to the location at 5 s on the flat plate where the vortex grazing was seen. The elevated temperature of the structure affects the flow by decreasing the density of the gas next to the model, therefore thickening the boundary layer. Figure 27a shows the thickening of the boundary layer profile on the windward side of the dome at the symmetry plane as time increases. As a consequence, the effective shape of the dome changes, increasing the extent and magnitude of the recirculation region. This is shown in Fig. 27b, where the boundary layer profile shows a taller recirculation region with stronger reversed flow. The thickening of the boundary layer changes both the velocity and temperature gradients at the surface so that the drag and heat load on the model evolve over time. The sum of the streamwise shear stress and pressure load, integrated over the surface of the model, gives the drag force. As the shear stress is affected by both the velocity gradient and the viscosity, which increases with temperature, the drag is calculated from the same flow field using two different viscosity models to investigate the modification of the flow field by the thermal solution. The baseline drag calculation uses temperature-dependent viscosity. The drag is again calculated from the same flow field using a constant viscosity model, where the viscosity is held at its freestream value, $\mu = \mu(T_\infty = 237.14\ \text{K})$. The results are shown in Table 3. The drag is seen to drop with time, but the drop is much smaller in the case of temperature-varying viscosity. The drag reduction with time in the constant viscosity case is due solely to the decreasing velocity gradient, which highlights the effect of the surface temperature on the boundary layer thickness. Also, as expected, the thickening boundary layer and increasing surface temperature cause the integrated heat load to decrease over time. A thermal-only simulation subject to a constant heat load (the initial heat load in the coupled case) yields a maximum surface temperature of 488 K. The temperature distribution on the centerline of the dome is shown in Fig. 28 for the two-way coupled and thermal-only simulations. The 23-K difference between the two cases demonstrates the integrated effect of the evolving heat load. The uncoupled peak temperature location also moves upstream relative to the coupled solution.

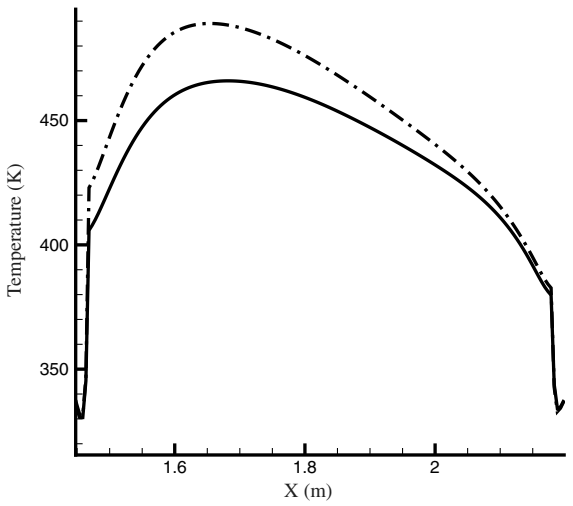

Fig. 28 Temperature along the centerline of dome: coupled (solid) and thermal-only (dashed) simulations.

V. Conclusion

A high-fidelity, coupled, fluid–thermal solver was developed for the thermal response prediction of extreme environment structures. For the purpose of solver validation, a hypersonic wind tunnel experiment was studied. The conditions inside the NASA Langley 8-Foot High Temperature Tunnel were reproduced to provide initial and boundary conditions for a coupled simulation. The solution filtering used in the simulation to promote numerical stability was observed to have an effect on the heat load calculation into the solid model. To minimize the impact of the filter on the coupled solution, a study was conducted to assess the effects of filtering on heat flux at the boundary of the fluid domain. Following that study, a coupled fluid–thermal simulation of hypersonic flow over a rigid structure was conducted over 5 s to compare with experimental data. Comparisons were made between simulations employing both a calorically perfect gas thermal model and a more general thermally perfect model, and the merits of each model were discussed. The impact of viscosity on the flow and, in particular, the surface heat flux resulting from vortical structures in the flow was investigated. The coupled simulation was run until 50 s, exceeding the available 5 s of experimental data, to evaluate the effect of fluid–thermal coupling on the fluid solution. The results of the simulation were also compared with predictions made using a semi-analytical model to highlight the similarities and differences of the two predictive approaches.

It was found that, if solution filtering is required to ensure numerical stability, the accuracy of the filter at the boundary can significantly affect heat flux by reducing the temperature gradient in the boundary layer. A comparison between results from our high-fidelity solver and a semi-analytical model based on inviscid aerodynamics and a flat plate boundary layer assumption revealed that, although qualitative trends of the heat loads were identified, a quantitative comparison shows a substantial overprediction by the simpler approach, with significant features in the heat flux not at all represented. Our simulations showed that the Reynolds analogy, a first-cut method for determining heat flux from surface shear stress, provides a fair estimate in hypersonic flows over a flat plate, but the method failed in the presence of pressure gradients. Thermal solution temperatures were found to be a function of heat load, geometry, and material properties. Our high-fidelity, coupled approach incorporated these aspects and produced solutions that were not obvious and may not be predicted by lower-order methods. It was also found that, in flows where there exist even isolated regions of extreme temperatures, the calorically perfect assumption may not be justified, requiring the use of a thermally perfect (or more general) gas model. Although changes in the fluid solution were not significant for the 5-s simulations, high temperatures that resulted from long periods of time in hypersonic flow had a noticeable effect on the flow solution in the coupled problem. This led to decreased drag and heat loads on the structure. The coupled solver predictions, using the thermally perfect gas model, were found to be within the experimental uncertainty for points on the dome interior, except for points near the dome periphery where details of the dome geometry were insufficiently described to be captured numerically.

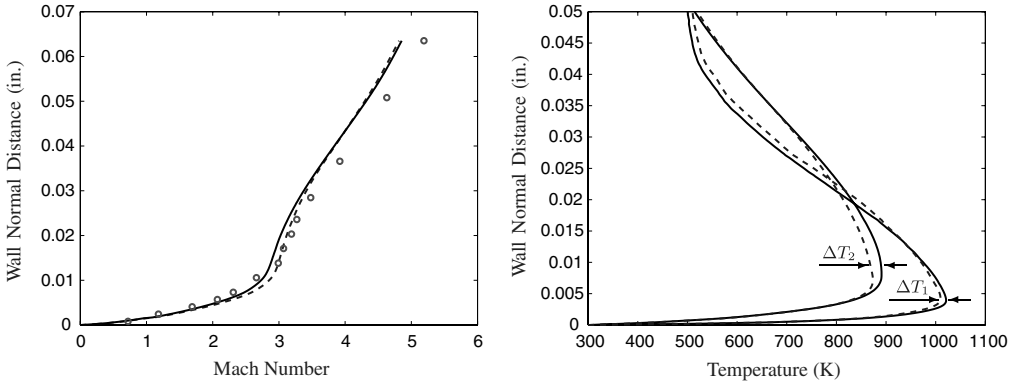

a) b)

Fig. A1 Calorically perfect (dashed line), thermally perfect (solid line), and experiment (circles): a) Boundary layer profile at $X = 1.476$ m and b) temperature profiles at $X_1 = 0.1$ m and $X_2 = 1.476$ m, where $\Delta T_1 = 11$ K and $\Delta T_2 = 17$ K.

Appendix: Comparison Between Gas Thermal Models with Equal Freestream Static Temperatures

To determine whether the more complex thermally perfect gas model would be justified if the calorically perfect case were run with freestream static temperature equal to that in the thermally perfect case ($T_\infty = 237.14$ K), an additional two-dimensional ANSYS Fluent simulation is run. The resulting flat plate heat flux and boundary layer profile are compared to those from the thermally perfect case. The calorically perfect and thermally perfect simulations are run on the same grid with the same freestream conditions.

The fluid in close proximity to the stagnation streamline passes through the high temperature region of the flow at the blunt leading edge where the calorically perfect and thermally perfect gas thermal models differ significantly. This is reflected in the surface heat flux at the blunt leading edge of the plate. At the stagnation point, the heat fluxes are 1107.1 kW/m^2 and 1024.1 kW/m^2 for the calorically perfect and thermally perfect cases, respectively. This result owes to the fact that the temperature of the gas in the stagnation region is higher in the calorically perfect case than in the thermally perfect case. The pressure and density are lower, leading to a larger shock standoff distance in the calorically perfect case. Accurate prediction of the flow in the stagnation region, heat flux in particular in design contexts, would require use of the more complex thermally perfect gas model.

Figure A1 shows the boundary layer and temperature profiles at the boundary layer probe location. Inside the boundary layer, Fig. A1a shows that, in the immediate vicinity of the plate, the thermally perfect model captures the near-wall gradients more closely than does the calorically perfect model. However, the differences are minor. It is interesting to note that, in Fig. A1b, the maximum temperature in the thermally perfect simulation is higher than that in the calorically perfect case. The heat flux into the flat region of the plate is shown in Fig. A2. Over the entire length of the plate, the calorically perfect model predicts a higher heat flux into the plate (approximately $+500$ W/m^2, $X = 0.25$ m), which decreases with distance (approximately $+15$ W/m^2, $X = 2.5$ m). In the calorically perfect case, more energy is lost to the plate over a given distance because of the higher heat flux predicted by the model, which causes a temperature difference between the two models in the boundary layer, which becomes larger with distance from the leading edge, as shown in Fig. A1b.

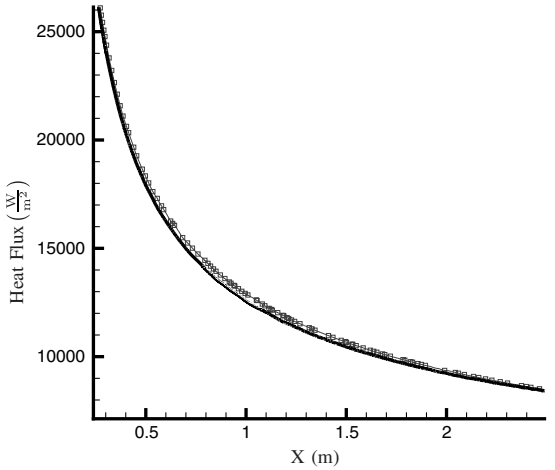

Fig. A2 Heat flux into the flat plate (W/m^2). Calorically perfect indicated by squares, thermally perfect indicated by solid line.

Acknowledgments

This work is supported by the U.S. Air Force Research Laboratory Air Vehicles Directorate under contract number FA8650-06-2-3620. Input from Dr. S. M. Spottswood, our technical monitor at AFRL (Wright–Patterson Air Force Base), is gratefully acknowledged. Support from the Illinois Space Grant Fellowship Program is also recognized. Computational resources were provided by the National Science Foundation Teragrid (TG-CTS090004) and on the DOD Distributed Shared Research Centers at ERDC and ARL. The authors also gratefully acknowledge the use of the parallel computing resource provided by the Computational Science and Engineering Program at the University of Illinois. Private communication with Dr. Christopher Glass was valuable and very much appreciated.

References

[1] Blevins, R. D., Holehouse, I., and Wentz, K. R., "Thermoacoustic Loads and Fatigue of Hypersonic Vehicle Skin Panels," *Journal of Aircraft*, Vol. 30, No. 6, 1993, pp. 971–978. doi:10.2514/3.46441

[2] Pozefsky, P., Blevins, R. D., and Laganelli, A. L., "Thermo-Vibro-Acoustic Loads and Fatigue of Hypersonic Flight Vehicle Structure," Flight Dynamics Lab., Air Force Research Lab., Rept. AFWAL-TR-89-3014, Wright-Patterson Air Force Base, OH, 1989.

[3] Beberniss, T., Eason, T., Gordon, B., Haney, M., Hollkamp, J., and Spottswood, M., "Response Prediction for Structures in Extreme Environments," TR, Structural Sciences Center, Air Force Research Lab./VAA, Wright-Patterson Air Force Base, OH, July 2007.

[4] Miles, J. W., "On Structural Fatigue under Random Loading," *Journal of the Acoustical Society of America*, Vol. 29, No. 1, 1957, p. 176.

[5] Blevins, R. D., "An Approximate Method for Sonic Fatigue Analysis of Plates and Shells," *Journal of Sound and Vibration*, Vol. 129, No. 1, 1989, pp. 51–71. doi:10.1016/0022-460X(89)90535-X

[6] Lyon, R. H., and Maidanik, G., "Statistical Methods in Vibration Analysis," *AIAA Journal*, Vol. 2, No. 6, 1964, pp. 1015–1024. doi:10.2514/3.2492

[7] Coe, C. F., Chyu, W. J., and Dods, J. B., "Pressure Fluctuations Underlying Attached and Separated Supersonic Turbulent Boundary Layers and Shock Waves," *AIAA Aeroacoustics Conference*, AIAA Paper 73-996, Oct. 1973.

[8] Zorumski, W. E., "Fluctuating Pressure Loads under High Speed Boundary Layers," NASA, Rept. TM-100517, Washington, D.C., 1987.
[9] Thompson, A. G. R., and Lambert, R. F., "The Estimation of RMS Stresses in Stiffened Skin Panels Subjected to Random Acoustic Loading," AGARD, Rept. AG-162, Neuilly Sur Seine, France, Nov. 1972.
[10] Chiu, W. K., Siovitz, U., Galea, S. C., and Koss, L. L., "Life Extension of Acoustically Fatigued Panels Using Add-On Dampers," *Composite Structures*, Vol. 44, Nos. 2–3, 1999, pp. 179–188. doi:10.1016/S0263-8223(98)00131-7
[11] Coate, J., and Meltzer, P. Jr., "AFRL Examines Technology Used to Test B-2 Aft Deck Performance," USAF Aeronautical Systems Center Press Release, State of Ohio Newsletter, 25 June 2008.
[12] Przekop, A., Rizzi, S. A., and Sweitzer, K. A., "An Investigation of High-Cycle Fatigue Models for Metallic Structures Exhibiting Snap-Through Response," *International Journal of Fatigue*, Vol. 30, No. 9, 2008, pp. 1579–1598. doi:10.1016/j.ijfatigue.2007.11.011
[13] Hollkamp, J. J., Gordon, R. W., and Spottswood, S. M., "Nonlinear Modal Models for Sonic Fatigue Prediction: A Comparison of Models," *Journal of Sound and Vibration*, Vol. 284, Nos. 3–5, 2005, pp. 1145–1163. doi:10.1016/j.jsv.2004.08.036
[14] Hollkamp, J., Beberniss, T., and Gordon, R., "The Nonlinear Response of a Plate to Acoustic Loading: Predictions and Experiments," AIAA Paper 2006-1928, 2006.
[15] Spottswood, S. M., and Allemang, R. J., "Identification of Nonlinear Parameters for Reduced Order Models," *Journal of Sound and Vibration*, Vol. 295, Nos. 1–2, 2006, pp. 226–245. doi:10.1016/j.jsv.2006.01.009
[16] Council, N. R., "Review and Evaluation of the Air Force Hypersonic Technology Program," AFSB, Rept. TR-J-97-01-A, National Academy Press, Washington, DC, 1998.
[17] Culler, A. J., and McNamara, J. J., "Studies on Fluid-Thermal-Structural Coupling for Aerothermoelasticity in Hypersonic Flow," *AIAA Journal*, Vol. 48, No. 8, 2010, pp. 1721–1738. doi:10.2514/1.J050193
[18] Culler, A., and McNamara, J., "Impact of Fluid-Thermal-Structural Coupling on Response Prediction of Hypersonic Skin Panels," *AIAA Journal*, Vol. 49, No. 11, 2011, pp. 2393–2406. doi:10.2514/1.J050617
[19] Lighthill, M. J., "Oscillating Airfoils at High Mach Numbers," *Journal of the Aeronautical Sciences*, Vol. 20, No. 6, June 1953, pp. 402–406. doi:10.2514/8.2657
[20] Eckert, E., "Engineering Relations for Heat Transfer and Friction in High-Velocity Laminar and Turbulent Boundary-Layer Flow over Surfaces with Constant Pressure and Temperature," *Journal of the Aeronautical Sciences*, Vol. 22, No. 8, 1955, pp. 585–587.
[21] Crowell, A., and McNamara, J., "Model Reduction of Computational Aerothermodynamics for Hypersonic Aerothermoelasticity," *AIAA Journal*, Vol. 50, No. 1, 2012, pp. 74–84. doi:10.2514/1.J051094
[22] Falkiewicz, N., and Cesnik, C., "Proper Orthogonal Decomposition for Reduced-Order Thermal Solution in Hypersonic Aerothermoelastic Simulations," *AIAA Journal*, Vol. 49, No. 5, 2011, pp. 994–1009. doi:10.2514/1.J050701
[23] Dechaumphai, P., Wieting, A., and Thornton, E., "Flow-Thermal-Structural Study of Aerodynamically Heated Leading Edges," *Journal of Spacecraft and Rockets*, Vol. 26, No. 4, 1989, pp. 201–209. doi:10.2514/3.26055
[24] Dechaumphai, P., Wieting, A. R., and Pandey, A., "Fluid-Thermal-Structural Interaction of Aerodynamically Heated Leading Edges," AIAA Archive Set 364, Jan. 1963. doi:10.2514/6.1989-1227
[25] Thornton, E., and Dechaumphai, P., "Coupled Flow, Thermal, and Structural Analysis of Aerodynamically Heated Panels," *Journal of Aircraft*, Vol. 25, No. 11, 1988, pp. 1052–1059. doi:10.2514/3.45702
[26] Kontinos, D. A., and Palmer, G., "Numerical Simulation of Metallic TPS Panel Bowing," *Journal of Spacecraft and Rockets*, Vol. 36, No. 6, 1997, pp. 842–849. doi:10.2514/2.3523
[27] Culler, A., and McNamara, J., "Coupled Flow-Thermal-Structural Analysis for Response Prediction of Hypersonic Vehicle Skin Panels," *51st AIAA/ASME/ASCE/AHS/ASC Structures, Structural Dynamics, and Materials Conference*, AIAA Paper 2010-2965, AIAA, Reston, VA, April 2010.
[28] Hassan, B., Kuntz, D., Salguero, D., and Potter, D., "A Coupled Fluid/Thermal/Flight Dynamics Approach for Predicting Hypersonic Vehicle Performance," AIAA Paper No. 2001-2903, 2001.
[29] Crowell, A., Miller, B., and McNamara, J., "Computational Modeling for Conjugate Heat Transfer of Shock-Surface Interactions on Compliant Skin Panels," *52nd AIAA/ASME/ASCE/AHS/ASC Structures, Structural Dynamics and Materials Conference*, AIAA Paper No. 2011-2017, Denver, Colorado, 4–7 April 2011.
[30] Zhao, X., Sun, Z., Teng, L., and Zheng, G., "Coupled Flow-Thermal-Structural Analysis of Hypersonic Aerodynamically Heated Cylindrical Leading Edge," *Engineering Applications of Computational Fluid Mechanics*, Vol. 5, No. 2, June 2011, pp. 170–179.
[31] Glass, C., and Hunt, L., "Aerothermal Tests of Spherical Dome Protuberances on a Flat Plate at a Mach Number of 6.5," NASA STI Recon Technical Report N, Vol. 87, Langley Research Center, Hampton, Virginia, 1986.
[32] Crowell, A., McNamara, J., and Miller, B. A., "Surrogate Based Reduced-Order Aerothermodynamic Modeling for Structural Response Prediction at High Mach Numbers," *52nd AIAA/ASME/ASCE/AHS/ASC Structures, Structural Dynamics and Materials Conference*, AIAA Paper 2011-2014, AIAA, Reston, VA, April 2011.
[33] Crowell, A., McNamara, J., Kecskemety, K., and Goerig, T., "A Reduced Order Aerothermodynamic Modeling Framework for Hypersonic Aerothermoelasticity," AIAA Paper 2010-2969, 2010.
[34] Vinokur, M., "Conservation Equations of Gasdynamics in Curvilinear Coordinate Systems," *Journal of Computational Physics*, Vol. 14, No. 2, 1974, pp. 105–125. doi:10.1016/0021-9991(74)90008-4
[35] Strand, B., "Summation by Parts for Finite Difference Approximations for D/Dx," *Journal of Computational Physics*, Vol. 110, No. 1, 1994, pp. 47–67. doi:10.1006/jcph.1994.1005
[36] Mattsson, K., Svärd, M., and Nordström, J., "Stable and Accurate Artificial Dissipation," *Journal of Scientific Computing*, Vol. 21, No. 1, 2004, pp. 57–79. doi:10.1023/B:JOMP.0000027955.75872.3f
[37] Carpenter, M. H., Gottlieb, D., and Abarbenel, S., "Time-Stable Boundary Conditions for Finite Difference Schemes Involving Hyperbolic Systems: Methodology and Application for High-Order Compact Schemes," *Journal of Computational Physics*, Vol. 111, No. 2, 1994, pp. 220–236. doi:10.1006/jcph.1994.1057
[38] Svärd, M., Carpenter, M. H., and Nordström, J., "A Stable High-Order Finite Difference Scheme for the Compressible Navier–Stokes Equations, Far-Field Boundary Conditions," *Journal of Computational Physics*, Vol. 225, No. 1, 2007, pp. 1020–1038. doi:10.1016/j.jcp.2007.01.023
[39] Svärd, M., and Nordström, J., "A Stable High-Order Finite Difference Scheme for the Compresible Navier–Stokes Equations: No-Slip Wall Boundary Conditions," *Journal of Computational Physics*, Vol. 227, No. 10, 2008, pp. 4805–4824. doi:10.1016/j.jcp.2007.12.028
[40] Nordström, J., Gong, J., der Weide, E. V., and Svärd, M., "A Stable and Conservative High Order Multi-block Method for the Compressible Navier–Stokes Equations," *Journal of Computational Physics*, Vol. 228, No. 24, 2009, pp. 9020–9035. doi:10.1016/j.jcp.2009.09.005
[41] Bodony, D. J., "Accuracy of the Simultaneous-Approximation-Term Boundary Condition for Time-Dependent Problems," *Journal of Scientific Computing*, Vol. 43, No. 1, 2010, pp. 118–133. doi:10.1007/s10915-010-9347-4
[42] Pulliam, T. H., and Chaussee, D. S., "A Diagonal Form of an Implicit Approximate-Factorization Algorithm," *Journal of Computational Physics*, Vol. 43, No. 2, 1981, pp. 357–372. doi:10.1016/0021-9991(81)90128-5
[43] Bodony, D. J., "Analysis of Sponge Zones for Computational Fluid Mechanics," *Journal of Computational Physics*, Vol. 212, No. 2, 2006, pp. 681–702. doi:10.1016/j.jcp.2005.07.014
[44] Lele, S. K., "Compact Finite Difference Schemes with Spectral-Like Resolution," *Journal of Computational Physics*, Vol. 103, No. 1, 1992, pp. 16–42. doi:10.1016/0021-9991(92)90324-R
[45] Kawai, S., Shankar, S., and Lele, S., "Assessment of Localized Artificial Diffusivity Scheme for Large-Eddy Simulation of Compressible Turbulent Flows," *Journal of Computational Physics*, Vol. 229, No. 5, 2010, pp. 1739–1762. doi:10.1016/j.jcp.2009.11.005
[46] Leyhe, E., and Howell, R., *Calculation Procedure for Thermodynamic, Transport, and Flow Properties of the Combustion Products of a Hydrocarbon Fuel Mixture Burned in Air with Results for Ethylene-*

Air and Methane-Air Mixtures, National Aeronautics and Space Administration, Washington, D.C., 1962.

[47] Kim, J., Bodony, D. J., and Freund, J. B., "LES Investigation of a Mach 1.3 Jet with and without Plasma Actuators," *47th Aerospace Sciences Meeting & Exhibit*, AIAA Paper 2009-0290, Jan. 2009.

[48] Bodony, D. J., "Heating Effects on the Structure of Noise Sources of High-Speed Jets," *47th Aerospace Sciences Meeting & Exhibit*, AIAA Paper 2009-0291, 2009.

[49] Sucheendran, M., Bodony, D. J., and Geubelle, P. H., "Structural-Acoustic Interaction of a Cavity-Backed, Clamped, Elastic Plate with Sound in a Duct," *Bulletin of the American Physical Society*, Vol. 54, No. 19, 2009.

[50] Zagaris, G., Bodony, D. J., Brandyberry, M., Campbell, M. T., Shaffer, E. G., and Freund, J. B., "A Collision Detection Approach to Chimera Grid Assembly for High Fidelity Simulations of Turbofan Noise," *48th AIAA Aerospace Sciences Meeting*, AIAA Paper 2010-836, Jan. 2010.

[51] Kim, J., Natarajan, M., Bodony, D. J., and Freund, J. B., "A High-Order, Overset Mesh Algorithm for Adjoint-Based Optimization for Aeroacoustics Control," *16th AIAA/CEAS Aeroacoustics Conference*, AIAA Paper 2010-3818, June 2010.

[52] Bodony, D. J., Zagaris, G., Reichert, A., and Zhang, Q., "Aeroacoustic Predictions in Complex Geometries," *Procedia Engineering*, IUTAM Symposium on Computational Aero-Acoustics for Aircraft Noise Prediction, Vol. 6, 2010, pp. 234–243.
doi:10.1016/j.proeng.2010.09.025

[53] Cook, D., Malkus, D. S., and Plesha, M., *Concepts and Applications of Finite Element Analysis*, Wiley, New York, 1974.

[54] Saad, Y., Schultz, M., "GMRES: A Generalized Minimal Residual Algorithm for Solving Nonsymmetric Linear Systems," *SIAM Journal on Scientific and Statistical Computing*, Vol. 7, No. 3, July 1986, pp. 856–869.
doi:10.1137/0907058

[55] Advanced CompuTational Software Collection, "Hypre," http://acts.nersc.gov/hypre/.

[56] Jaiman, R., Jiao, X., Geubelle, P., and Loth, E., "Assessment of Conservative Load Transfer for Fluid-Solid Interface with Non-matching Meshes," *International Journal for Numerical Methods in Engineering*, Vol. 64, No. 15, 2005, pp. 2014–2038.
doi:10.1002/nme.1434

[57] Jaiman, R., Jiao, X., Geubelle, P., and Loth, E., "Conservative Load Transfer Along Curved Fluid-Solid Interface with Non-matching Meshes," *Journal of Computational Physics*, Vol. 218, No. 1, 2006, pp. 372–397.
doi:10.1016/j.jcp.2006.02.016

[58] Giles, M. B., "Stability Analysis of Numerical Interface Conditions in Fluid-Structure Thermal Analysis," *International Journal for Numerical Methods in Fluids*, Vol. 25, No. 8, 1997, pp. 421–436.
doi:10.1002/(SICI)1097-0363(19970830)25:4<421::AID-FLD557>3.0.CO;2-J

[59] Roe, B., Haselbacher, A., and Geubelle, P. H., "Stability of Fluid-Structure Thermal Simulations on Moving Grids," *International Journal for Numerical Methods in Fluids*, Vol. 54, No. 9, 2007, pp. 1097–1117.
doi:10.1002/fld.1416

[60] Ostoich, C., Bodony, D. J., and Geubelle, P. H., "Thermal Loads on a Domed Protuberance under a Mach 5.7 Boundary Layer," *Bulletin of the American Physical Society*, Vol. 56, No. 18, 2011.

[61] Jameson, A., "Transonic Flow Calculations for Aircraft," *Numerical Methods in Fluid Dynamics. Lecture Notes in Mathematics Volume 1127*, edited by F. Brezzi, Springer–Verlag, New York, 1985.

[62] Swanson, R. C., and Turkel, E., "Multistage Schemes with Multigrid for Euler and Navier–Stokes Equations," NASA, TR-3631, Washington, D.C., Aug. 1997.

[63] Glass, C., and Hunt, L., "Aerothermal Tests of Quilted Dome Models on a Flat Plate at a Mach Number of 6.5," NASA STI Recon Technical Report N, Vol. 88, Langley Research Center, Hampton, Virginia, 1988.

[64] Hodge, J., and Harvin, S., "Test Capabilities and Recent Experiences in the NASA Langley 8-Foot High Temperature Tunnel," *21st AIAA Advanced Measurement Technology and Ground Testing Converence*, AIAA Paper 2000-2646, June 2000.

[65] Dandy, D., Chemical Equilibrium Calculation, Colorado State Universiy Bioanalytical Microfluidics Program, 2012, http://navier.-engr.colostate.edu/~dandy/ [retrieved 20 Sept. 2012].

[66] Huebner, L., Rock, K., Voland, R., and Wieting, A., "Calibration of the Langley 8-Foot High Temperature Tunnel for Hypersonic Airbreathing Propulsion Testing," *19th AIAA Advanced Measurement and Ground Testing Technology Conference*, New Orleans, Louisiana, AIAA Paper 1996-2197, June 1996.

[67] Harris, J., and Blanchard, D., "Computer Program for Solving Laminar, Transitional, or Turbulent Compressible Boundary-Layer Equations for Two-Dimensional and Axisymmetric Flow," NASA STI Recon Technical Report N, Vol. 83, Langley Research Center, Hampton, Virginia, 1982.

[68] Ostoich, C., Bodony, D. J., and Geubelle, P. H., "Development and Validation of a First Principles Fluid-Thermal Multi-physics Solver for Hypersonic Boundary Layer Heat Transfer Problems," *13th AIAA Dynamic Specialists Conference*, AIAA Paper 2011-1964, Denver, Colorado, 4–7 April 2011.

[69] Omega Engineering, Inc., "Reference Tables for Standard Type K Thermocouples," http://www.omega.com/temperature/Z/pdf/z204-206.pdf [retrieved 30 Jan. 2012].

L. Tichy
Associate Editor